

1       **On the Nationwide Variability of Low-Level Jets Prior**  
2       **to Warm-season Nocturnal Rainfall in China Revealed**  
3       **by Radar Wind Profilers**

4       Ning Li<sup>a,b,c</sup>, Jianping Guo<sup>a,d\*</sup>, Xiaoran Guo<sup>a,d</sup>, Tianmeng Chen<sup>a,d</sup>, Zhen Zhang<sup>a</sup>, Na  
5       Tang<sup>a</sup>, Yifei Wang<sup>a</sup>, Honglong Yang<sup>d</sup>, Yongguang Zheng<sup>c</sup>, Yongshui Zhou<sup>c</sup>

6       <sup>a</sup> *State Key Laboratory of Severe Weather Meteorological Science and Technology &*  
7       *Specialized Meteorological Support Technology Research Center, Chinese Academy*  
8       *of Meteorological Sciences, Beijing 100081, China*

9       <sup>b</sup> *College of Earth and Planetary Sciences, University of Chinese Academy of*  
10       *Sciences, Beijing 100049, China*

11       <sup>c</sup> *National Meteorological Centre, Beijing 100081, China*

12       <sup>d</sup> *CMA Field Scientific Experiment Base for Low-Altitude Economy Meteorological*  
13       *Support of Unmanned Aviation in Guangdong-Hong Kong-Macao Greater Bay Area,*  
14       *Shenzhen 518108, China*

15       <sup>e</sup> *Guizhou Meteorological Observatory, Guiyang 550001, China*

16  
17  
18  
19  
20  
21       Correspondence to:

22       Dr./Prof. Jianping Guo (Email: [jpguocams@gmail.com](mailto:jpguocams@gmail.com))

23



## Abstract

25  
26  
27  
28  
29  
30  
31  
32  
33  
34  
35  
36  
37  
38  
39  
40  
41  
42  
43  
44  
45  
46  
47  
48

Nocturnal rainfall initiation is closely linked to low-level jets (LLJs), but national-scale LLJ features over China—especially their evolution preceding warm-season nocturnal rainfall—remain unknown due to scarce high-resolution vertical observations. Here, we reveal the fine vertical structure of LLJs and their rapid evolution within 2 hours preceding the onset of nocturnal heavy rain (HR) and non-HR across four phases of rainy seasons in China during the warm season (April–October) of 2023–2024, utilizing data from a nationwide network of radar wind profilers (RWPs) in combination with surface observations and reanalysis data. Results show that nocturnal rainfall accounted for over 50% of warm-season rainfall, with 56% preceded by LLJs within 2 hours of its onset. In monsoon regions, ~45% of nocturnal HR were LLJ-associated (LLJ\_HR), producing heavier rainfall than non-LLJ\_HR events. Critically, LLJ\_HR events underwent a minute-scale ‘rapid reorganization’ of the LLJ structure, characterized by oscillatory evolution in jet height, frequency and strength. This creates a favorable environment for the ‘final-stage intensification’ of dynamic field during the last ~30 min, where widespread intensification of jet—coupled with significant thermodynamic instability—act as a primary dynamical forcing mechanism and a key precursor signal for HR initiation. In stark contrast, LLJ\_non-HR events exhibited quasi-steady or weakening dynamical trends, accompanied by an inadequate thermodynamic response that lacks such synergistic coupling. These findings demonstrate that minute-scale dynamic adjustments driven by swift evolution of the LLJ are essential for nocturnal HR, offering critical observational constraints for regional model parameterizations and nowcasting accuracy.

## Short Summary

49

50 Nighttime rainfall often links to low-level jets (LLJs), but we lack clarity on nationwide  
51 LLJ features. We here used a nationwide radar wind profiler network to study LLJ  
52 changes 2 hours before rainfall, covering China's 2023–2024 rainy seasons. 56%  
53 nighttime rainfall had LLJs. The LLJs-associated heavy rain needed a rapid adjustment  
54 of LLJs' vertical structure, especially a significant intensification within 30 minutes  
55 preceding rain. This shows the importance of LLJ in nowcasting rainfall.

56

57

58

59

60

61

62

63

64

## 65 **1. Introduction**

66 Forecasting nocturnal heavy rainfall (HR) and associated severe convective  
67 weather remains a major challenge in hazardous weather prediction (Davis et al., 2003;  
68 Trier et al., 2006), owing to the complexity of triggering mechanisms, the scarcity of  
69 continuous high-resolution observations, and inaccuracies in model parameterizations  
70 (Carbone and Tuttle, 2008; Reif and Bluestein, 2017; Weckwerth et al., 2019; Zhao et  
71 al., 2025). Crucially, the low-level jet (LLJ) that exhibit a diurnal cycle with a  
72 maximum at night is widely recognized as a key contributor to nocturnal HR (Bonner  
73 1968; Mitchell et al., 1995; Tuttle and Davis, 2006), as documented in regions or  
74 countries such as the Great Plains of the United States (Maddox, 1983; Higgins et al.,  
75 1997), Argentina (Marengo et al., 2004), India (Monaghan et al., 2010), North China  
76 Plain (Li et al., 2024).

77 The LLJs primarily originate from the inertial oscillations (IO) following the  
78 sudden decay of turbulence after sunset (Blackadar, 1957) and thermal imbalances  
79 induced baroclinicity over sloping terrain (Holton, 1967). Functioning as concentrated  
80 corridors for heat, moisture, and momentum transport, LLJs can modulate the diurnal  
81 oscillation in water vapor by IO (Rasmusson, 1967; Zhang et al., 2019) and enhance  
82 convective instability, particularly when elevated high- $\theta_e$  air encounters frontal  
83 boundaries (Trier et al., 2017). Also, strong low-level vertical wind shear (VWS)  
84 associated with LLJs necessarily benefits deep lifting (Maddox et al., 1979; Stensrud,  
85 1996; Rasmussen and Houze, 2016). These mechanisms collectively provide essential  
86 thermodynamic and dynamic support for the initiation and organization of nocturnal  
87 convection, especially where LLJs force low-level ascent at jet termini or via positive  
88 vorticity advection left of the jet axis (Chen et al., 2017; Du and Chen, 2019; Xia and  
89 Zhao, 2009).

90 Furthermore, LLJs interact synergistically with other key factors to trigger HR that  
91 is associated with mesoscale convective systems (Chen et al. 2010; Chen et al., 2017;  
92 Chen et al., 2024), including terrain effects (Anthes et al., 1982; Pan and Chen, 2019;  
93 Huang et al., 2020), gravity waves (Weckwerth & Wakimoto, 1992), among others.

94 These interactions are highly sensitive to the prevailing synoptic and subsynoptic-scale  
95 environmental conditions (e.g., Hodges and Pu, 2019) and fine-scale structural of LLJs,  
96 including LLJ frequency, spatial redistribution, and particularly localized wind profile  
97 accelerations (Pitchford and London, 1962; Walters and Winkler, 2008; Du and Chen,  
98 2019; Li et al., 2024). Understanding these intricate evolution features of LLJs is critical  
99 for improving the forecasting of nocturnal HR.

100 Despite advances facilitated by regional reanalysis (e.g., Doubler et al., 2015; Li  
101 et al., 2021), numerical modeling (e.g., Zhang and Meng, 2019), radiosonde  
102 observations (e.g., Whiteman et al., 1997; Yan et al., 2020), and emerging artificial  
103 intelligence techniques (e.g., Subrahmanyam et al., 2024) in understanding the  
104 climatology and physical mechanisms of LLJs and their role in HR forecasting,  
105 significant knowledge gaps remain. The insufficient spatiotemporal resolution of  
106 conventional observing systems limits the ability to capture rapid pre-storm  
107 environmental changes (Weisman et al., 2015; Cao et al., 2025; Roots et al., 2025),  
108 thereby hindering systematic analysis of the fine-scale structure of LLJs and their  
109 minute-scale evolution within the critical 2-hour window preceding rainfall.

110 Moreover, the mechanisms and impacts of LLJs exhibit considerable variation  
111 across monsoon phases and geographic regions. As a classic monsoon climate region,  
112 China exhibits particularly prominent nocturnal rainfall contributions across major  
113 climate-sensitive areas (Yu et al., 2014), where LLJs play a crucial role in modulating  
114 primary rainfall belts (Sun, 1986; Chen et al., 2010; Wang et al., 2013; Horinouchi et  
115 al., 2019), such as those in Eastern China (Chen et al., 2017; Xue et al., 2018) and South  
116 China (Du et al., 2020; Bai et al., 2021; Fu et al., 2021). However, nationwide  
117 comparative studies examining LLJ precursor signals across different monsoon phases  
118 in China are still lacking.

119 Radar wind profilers (RWPs) can offer transformative potential by capturing  
120 minute-resolution wind profiles to reveal pre-rainfall dynamic precursors (Zamora et  
121 al., 1987; Du et al., 2012; Molod et al., 2019; Guo et al., 2023). For example, Gebauer  
122 et al. (2018) demonstrated the capability of RWPs to elucidate how heterogeneous  
123 structures of LLJ trigger nocturnal convection in Great Plains; Based on a linear net of

124 RWPs deployed across the North China Plain, our previous study (Li et al., 2024)  
125 observed rapid intensification of moisture flux convergence (MFC) driven by a surge  
126 in LLJs profile within 30 min preceding nocturnal rainfall onset, highlighting the  
127 sensitivity of RWP to minute-scale perturbations of LLJs profiles. However, it remains  
128 an open question whether this minute-scale precursor is universally applicable across  
129 diverse monsoon phases throughout mainland China. Furthermore, the systematic  
130 differences in the fine-scale LLJ evolution that distinguish HR from non-HR have yet  
131 to be fully elucidated.

132 Therefore, this study utilizes a nationwide network of RWPs to address the  
133 following two questions: 1) How do the vertical structure of LLJs and their minute-  
134 scale evolution within 0–2 hours preceding nocturnal rainfall vary across different rainy  
135 season phases? and 2) What are the systematic differences in LLJ dynamic-  
136 thermodynamic mechanisms between LLJ-influenced HR and non-HR events? The  
137 remainder of this paper is structured as follows: Section 2 details data and methodology,  
138 Section 3 presents comparative analyses of characteristics of rainfall and LLJs  
139 evolution, and Section 4 synthesizes key conclusions.

## 140 **2. Data and Methodology**

### 141 *2.1 Radar wind profiler measurements*

142 The RWP observations collected from 31 stations across China (Fig.1) from April  
143 to October in 2023–2024 were analyzed in this study, which can provide wind speed  
144 and direction with a vertical resolution of 120 m and an interval of 6 minutes (Liu et al.,  
145 2019). To reduce the potential influence of poor data quality, RWP data underwent  
146 strict quality control following procedures proposed by Wei et al. (2014) and Miao et  
147 al. (2018). Firstly, to minimize contamination from precipitation particles, which can  
148 introduce significant errors in Doppler-based wind retrieval, all observations during  
149 rainfall periods were removed. Secondly, within each profile below 3 km above ground  
150 level (AGL), missing values and significant outliers that were defined as values  
151 exceeding 2.5 standard deviations from the mean were removed. Next, for each profile,  
152 if more than 40% of the data points below 3 km AGL were outliers or missing, that

153 entire profile was discarded. Finally, discontinuous, or missing data points were  
154 estimated using linear interpolation. Following this quality control process, 109,400  
155 wind profiles were discarded and a total of 2,606,042 profiles across China were  
156 available for analysis during the study period.

## 157 *2.2 Multi-source meteorological data*

158 In addition, 1-min rainfall measurements were directly acquired from the rain  
159 gauge measurements at 2160 national weather stations across China to identify rainfall  
160 events. Rainfall amounts were accumulated over 6-min intervals to ensure temporal  
161 alignment with the RWP measurements. Ground-based meteorological variables are  
162 measured at 1-min intervals from national weather stations, including 2-m air  
163 temperature, relative humidity, and surface pressure. All ground-based data have  
164 undergone rigorous quality control (China Meteorological Administration, 2020; Zhao  
165 et al., 2024) and are publicly accessible at the National Meteorological Information  
166 Center of China Meteorological Administration (CMA).

167 Furthermore, to diagnose large-scale circulation patterns and environmental  
168 conditions preceding nocturnal rainfall influenced by LLJs, this study utilized  
169 meteorological variables derived from the fifth generation of the European Centre for  
170 Medium-Range Weather Forecasts atmospheric reanalysis (ERA5) of the global  
171 climate (Hersbach et al., 2020). The ERA5 data features a horizontal resolution of  
172  $0.25^{\circ} \times 0.25^{\circ}$  across 37 vertical pressure levels and hourly temporal resolution. Unless  
173 otherwise specified, all datasets cover the study period of April to October in 2023–  
174 2024.

## 175 *2.3 Identification of nocturnal rainfall events*

176 Firstly, days with typhoon activity were excluded. To minimize the impact of  
177 rainfall on RWP measurements, a minimum dry interval of 2 hours was required  
178 between consecutive rainfall events. Following the methodology of Li et al. (2024), a  
179 rainfall occurrence was defined when the accumulated rainfall measured by all rain  
180 gauges within a 25-km radius of each RWP station exceeded 0.1 mm. To account for

181 rainfall intermittency and filter out transient noise, a valid rainfall event required the  
182 initial detection to be followed by at least two subsequent occurrences within 30 min.  
183 Any isolated initial occurrence not meeting this criterion was discarded. Notably, this  
184 25-km radius serves as a rigorous spatial constraint to not only mitigates the limitations  
185 of single-gauge measurements but also ensures the onset of rainfall at this scale are  
186 temporally coherent with that of the rain gauge co-located with RWP (as confirmed by  
187 sensitivity tests in Fig. S1 and Table S1). This guarantees direct physical coupling  
188 between local rainfall and the RWP-observed wind profiles.

189 Nocturnal rainfall events were defined as those occurring between 2000 and 0800  
190 Local Standard Time (LST). Based on operational classifications from the National  
191 Water Resources Bureau and CMA, the rainy season was categorized into four  
192 consecutive phases: (1) the South China Pre-summer Rainy Season (April 1 to June 8,  
193 2023 and April 1 to June 9, 2024), (2) the Meiyu Season (June 9 to July 14, 2023 and  
194 June 10 to July 21, 2024), (3) the North China Rainy Season (July 15 to August 31,  
195 2023 and July 22 to August 31, 2024), and (4) the West China Autumn Rainy Season  
196 (September 1 to October 31 for both 2023 and 2024). These phases are subsequently  
197 designated as Phase 1 to Phase 4 throughout this study. Four regions of interest (ROIs)  
198 were subsequently selected for detailed analysis (see Table 1).

199 Further screening identified locally nocturnal HR events, where the mean 6-min  
200 rainfall intensity exceeded the 75th percentile of all recorded rainfall events at each  
201 station. This threshold can effectively distinguish significant HR from weak rainfall  
202 while ensuring a sufficient sample size for robust statistical analysis of minute-scale  
203 LLJ dynamics (Table S1). Furthermore, a sensitivity test by varying the thresholds to  
204 85th and 95th percentile to ensure that the main conclusion regarding the precursory  
205 signals of LLJs is robust within a reasonable threshold range (see Figs. S2–S5).

206 Statistical analysis revealed 3,155 nocturnal rainfall events during the 2023–2024  
207 warm seasons (within the 31 red circles shown in Fig.1). Event counts per rainy season  
208 phase were 1,109, 689, 652, and 705 respectively, with 841 events classified as  
209 nocturnal HR events.

## 210 *2.4 Identification of LLJs and associated rainfall event*

211 To ensure identified LLJs exhibit significant vertical wind shear characteristic of  
212 jet-like profiles, the following criteria are adopted: (1) a maximum horizontal wind  
213 speed exceeding  $10 \text{ m s}^{-1}$  in the lowest 3 km AGL, and (2) a wind speed reduction of  
214 at least  $3 \text{ m s}^{-1}$  from the maximum to minimum below 3 km AGL, or to 3 km AGL if  
215 no minimum exists. These deliberately conservative wind speed thresholds maximize  
216 LLJ sample size for enhanced statistical robustness. This definition standard has been  
217 widely adopted in previous studies (Bonner, 1968; Whiteman et al., 1997; Du et al.,  
218 2014; Yan et al., 2020). The strength of LLJ or jet nose is defined as the maximum wind  
219 speed along the entire profile. The LLJ core height is defined as the altitude of the wind  
220 speed maximum during LLJ occurrences. Correspondingly, the LLJ direction is  
221 determined by the wind direction at the height of the LLJ.

222 We define rainfall events where LLJ occurs at least twice within 2 hours before rainfall  
223 as an LLJ event (Li et al., 2024). The HR events influenced by LLJs (LLJ\_HR events),  
224 HR events without LLJ influence (non-LLJ\_HR events), and non-HR events affected  
225 by LLJ (LLJ\_non-HR events) are further distinguished.

## 226 **3. Results and discussion**

### 227 *3.1 General characteristics of nocturnal rainfall and LLJs*

228 Firstly, we characterized the spatiotemporal patterns of rainfall and LLJs observed  
229 nationwide during the 2023-2024 warm season. Nationally, nocturnal rainfall  
230 accounted for 50.9% of total warm-season rainfall, with pronounced concentrations  
231 over North, Northeast and Southwest China (Figs. 2d and 2g). In contrast, the  
232 pronounced daytime rainfall dominance in South China (Fig. 2a) may arise from the  
233 interaction between enhanced onshore monsoonal flows and terrain (Bai et al., 2020),  
234 sea breeze fronts and cold pool (Chen et al., 2016). In terms of frequency, nocturnal  
235 rainfall occurred more frequently, constituting 52.5% of the total rainfall frequency  
236 versus 47.5% for the daytime, with the highest nocturnal proportions found in  
237 southwestern and eastern regions (Figs. 2e and 2h). Although the national mean rainfall

238 intensity was generally lower at night (1.2 mm/h) than during the day (1.8 mm/h; Figs.  
239 2c and 2f), the probability of nocturnal HR occurrence was significant (51.3%),  
240 particularly across western, North, and northeastern China (Fig. 2i).

241 Figure 3 displays the key attributes of LLJs detected at all 31 RWP across China  
242 using the criteria defined in Section 2. Nocturnal LLJ activity occurred more frequently,  
243 with an overall occurrence frequency increase of nearly 18% relative to diurnal LLJs  
244 (Figs. 3a and 3e). This pronounced nighttime enhancement is consistent with the  
245 classical IO mechanism, whereby reduced surface friction after sunset allows the  
246 decoupled boundary layer to accelerate and form stronger LLJs. Spatially, both daytime  
247 and nighttime LLJs were more prevalent in eastern and southeastern China, particularly  
248 along the Yangtze River basin and coastal regions, where moisture-rich monsoonal  
249 flows dominate. In contrast, lower frequencies were observed over northwestern China,  
250 likely reflecting weaker large-scale moisture transport and reduced baroclinicity in arid  
251 inland regions.

252 In terms of jet core height (Figs. 3b and 3f), nocturnal LLJs generally exhibited  
253 slightly lower core altitudes compared to their daytime counterparts, with most cores  
254 concentrated below  $\sim 1500$  m. This lowering of the jet core at night is consistent with  
255 boundary-layer stabilization and the formation of a shallow nocturnal inversion, which  
256 confines the jet maximum to lower altitudes. Regarding jet intensity (Figs. 3c and 3g),  
257 nighttime LLJs were typically stronger, with a higher proportion of stations reporting  
258 wind speeds exceeding  $16\text{--}18\text{ m s}^{-1}$ . The combination of enhanced wind speed and  
259 reduced core height suggests a more concentrated and dynamically organized jet  
260 structure during nighttime hours. The dominant wind directions (Figs. 3d and 3h)  
261 further reflect regional circulation controls. Southeasterly and southwesterly LLJs  
262 prevailed in eastern China, consistent with the transport of warm, moist air from the  
263 South China Sea and western Pacific during the warm season. In northern and  
264 northwestern regions, LLJs exhibited more variable directional characteristics, likely  
265 influenced by synoptic-scale pressure gradients and topographic channeling effects.

266 Overall, Fig. 3 demonstrates that nocturnal LLJs are not only more frequent but  
267 also stronger and lower in altitude than their daytime counterparts. These structural  
268 differences imply enhanced moisture transport efficiency and greater potential for  
269 nighttime convective organization, providing a dynamical foundation for the observed  
270 diurnal asymmetry in heavy rainfall occurrence examined in subsequent sections.

271 Statistical analysis revealed a substantial linkage between LLJs and nocturnal  
272 rainfall. Specifically, 56% of all nocturnal rainfall events across China were preceded  
273 by the presence of LLJs within 2 hours, establishing nocturnal rainfall influenced by  
274 LLJs as a major component of warm-season rainfall in China. This relationship was  
275 strongly modulated by the seasonal migration of the western Pacific subtropical high  
276 (WPSH), whose northward progression and subsequent retreat governed the latitudinal  
277 displacement of HR belts and closely synchronized with the spatiotemporal evolution  
278 of LLJ activity. The proportion of nocturnal rainfall events associated with LLJs during  
279 the four rainy season phases reached 60.4%, 56.3%, 49.4%, and 54.9%, respectively  
280 (solid-filled bars in Fig. 4a). Among 841 identified nocturnal HR events nationwide,  
281 33.9%–47.2% were classified as LLJ\_HR events across the four phases (diagonally  
282 striped bars in Fig. 4a). This contrast between the high LLJ association for general  
283 nocturnal rainfall and the more moderate fraction for HR indicates that, although LLJs  
284 are a frequent precursor to rainfall, their presence alone does not guarantee the  
285 occurrence of heavy rainfall.

286 A more detailed statistical analysis of ROIs revealed the key role of LLJ coupling  
287 in primary rain belt regions of each phase. A total of 71, 49, 33, and 34 nocturnal HR  
288 events were identified in these ROIs during the period from Phase 1 to Phase 4 (Fig.  
289 4b). On average, nearly 45.0% of HR events in these regions were associated with LLJs  
290 within 2 hours before onset. Spatial analysis further confirmed that these LLJ\_HR  
291 events consistently produced heavier rainfall intensities than non-LLJ\_HR events (red  
292 boxes in Fig. 5), particularly within the four ROIs (red boxes in Fig. 5). Nevertheless,  
293 the non-LLJ\_HR events exhibited spatially heterogeneous intensity distributions,  
294 where localized maxima may occur in areas outside the primary rain belts. For instance,  
295 during Phase 2 in ROI-3 (Fig. 5f), sporadic high-intensity events driven by deep cold

296 trough system resulted in high site-averaged intensities even without LLJs, whereas in  
297 ROI-2, the absence of LLJs typically corresponded to weaker frontal precipitation (Fig.  
298 S6).

299 Furthermore, at the national scale, probability distributions of rainfall intensity  
300 (Fig. 6) indicated that LLJ\_HR events exhibited a significantly higher tail ( $\geq 2.0$  mm/6  
301 min) compared to non-LLJ\_HR events during Phases 1 and 3. During Phases 2 and 4,  
302 however, the distributions of the two event types were comparable, with LLJ\_HR  
303 events showing slightly weaker intensities. Regionally, rainfall intensities within the  
304 key ROIs generally exceeded the national average, particularly for LLJ\_HR events.  
305 Specifically, ROI-1 and ROI-2 demonstrated significantly higher probabilities of  
306 heavier rainfall ( $\geq 2.0$  mm/6 min) in LLJ\_HR events. Notably, LLJ\_HR events in  
307 ROI-4 favored intensities near 0.5 and 2.8 mm/6 min, yet the overall probabilities of  
308 heavier rainfall remained slightly lower than non-LLJ\_HR events. Despite the  
309 relatively high frequency of LLJ\_HR events in ROI-3 during Phase 3 (see the pie charts  
310 in Fig. 6), their probability of producing heavier rainfall was comparable to—rather  
311 than substantially greater than—that of non-LLJ\_HR events. Moreover, this region  
312 exhibited the sharpest decay in probability density for heavier rainfall among all regions.  
313 This behavior suggests that, although LLJs occur frequently in this region and season,  
314 their contribution to extreme rainfall intensity is not dominant. Instead, other non-LLJ  
315 forcing mechanisms, such as topographic lifting and mesoscale convective systems,  
316 may play an equally or more significant role in generating HR in ROI-3 during Phase  
317 3.

318 In summary, although LLJ\_HR events were generally associated with enhanced  
319 rainfall intensities across most ROIs and most phases, only  $\sim 31.1\%$  of all identified LLJ  
320 events were ultimately classified as HR events (Fig. 4b). This relatively low conversion  
321 rate indicates that the mere presence of LLJs is not sufficient to produce HR. The  
322 substantial number of LLJ\_non-HR events implies that additional dynamic and  
323 thermodynamic conditions must coexist with LLJs to trigger HR. In particular, factors  
324 such as moisture transport efficiency, vertical wind shear configuration, atmospheric  
325 stability, and mesoscale lifting mechanisms may modulate whether an LLJ evolves into

326 a heavy-rain-producing system. Therefore, a detailed further examination of the fine-  
327 scale vertical structures of LLJs prior to rainfall onset is crucial to disentangle the  
328 dynamical characteristics that distinguish HR-producing LLJs from non-HR cases, as  
329 explored in the following sections.

### 330 *3.2 Minute-scale evolution of LLJs preceding nocturnal heavy and non-heavy* 331 *rainfall*

332 To elucidate the contrasting precursor characteristics of LLJs that lead to nocturnal  
333 rainfall of differing intensities, this section examines fine-scale vertical structure and  
334 continuous evolution of LLJs within 2 hours preceding both LLJ\_HR and LLJ\_non-HR  
335 events during four phases in their respective ROIs. The results revealed the distinct  
336 spatiotemporal variations in vertical structure and evolutionary patterns of LLJs  
337 occurred across seasonal phases.

338 During Phase1 in ROI-1, LLJ\_HR events exhibited a significant increase in  
339 frequency starting 108 min before rainfall onset, reaching secondary peaks at –84 min  
340 and –60 min, culminating in maximum frequency immediately preceding HR (Fig. 7a).  
341 Meanwhile, the average wind profiles showed a rapid intensify trend from 48 min  
342 before HR onset, with the jet core reaching its peak wind speed (about  $12.2 \text{ m s}^{-1}$ ) and  
343 its height distinctly decreased (Fig. 8a), although there is the transient weakening of jet  
344 strength within 60–48 min preceding HR. These LLJs featured a bimodal vertical  
345 distribution with frequent occurrence layers at 0.5–1 km and 1.5–2 km AGL. This  
346 structure was characteristic of double low-level jets (DLLJs), where the coexistence of  
347 the boundary layer jets (BLJs) and synoptic-system-related jets (SLLJs) generated a  
348 deep layer of forced ascent via BLJ-exit convergence and SLLJ-entrance divergence.  
349 This dynamical coupling significantly favors organized deep convection in ROI-1  
350 (Uccellini and Johnson, 1979; Du and Chen, 2018; Du and Chen, 2019; Liu et al., 2020).  
351 Note that the composite wind profile (Fig. 8a) does not show a distinct bimodal vertical  
352 distribution due to smoothing from averaging. Detailed examination of wind profiles  
353 revealed that approximately 40% of LLJ\_HR events exhibited DLLJs, while only 20%  
354 of LLJ\_non-HR events showed such a structure. Therefore, LLJ\_non-HR events lacked

355 this dynamic coupling, with jets predominantly confined to the single 0.5–1 km layer.  
356 Although LLJ\_non-HR events showed a gradual increase in frequency from –48 min,  
357 along with strengthening winds prior to rainfall (Figs. 7e and 8e), these changes were  
358 rather limited compared to the pronounced evolution seen in LLJ\_HR events under a  
359 background of overall lower frequency and weaker intensity. This steady and weak  
360 dynamical structure failed to provide sufficient dynamic lifting to efficiently initiate  
361 strong convection.

362 Both event types exhibited notably high frequencies and intensities of LLJs over  
363 ROI-2 during Phase 2, yet their evolutionary dynamics diverged sharply. For LLJ\_HR  
364 events, a coherent oscillatory vertical reorganization of LLJs is evident (Figs. 7b and  
365 8b). At the first stage, both LLJ frequency and wind speed maximum peaked (exceeding  
366  $12 \text{ m s}^{-1}$ ) at –120 min, with the core situated 1.5–2 km AGL. Subsequently, a rapid  
367 descent of frequently occurring height of LLJs to below 1 km AGL occurred,  
368 accompanied by a concurrent decline in frequency and profile intensity to a minimum  
369 around 84–72 min preceding HR. Analysis of wind kinetic energy and its vertical  
370 transport (see Eqs. 1 and 2 in supporting material) confirmed that the ‘sudden drop’  
371 likely results from the downward momentum transfer (Fig. S7a and c), which can  
372 efficiently enhance low-level disturbances and dynamic forcing and serve as an  
373 effective indicator of HR 1–2 hours later (Liu et al. 2003; Fu et al., 2020). Following  
374 this descent, a distinct recovery phase ensued from –60 min, where the frequency  
375 increased reaching a secondary peak at –48 min and jet core re-ascended to 1–2 km  
376 AGL. The LLJ profile strength re-intensified to about  $11.4 \text{ m s}^{-1}$ . This rise of the jet  
377 core and secondary enhancement are likely tied to cold pool-LLJ interactions and  
378 intensified upward motion or latent heat release in convective clouds (further discussed  
379 in Section 3.3). In conclusion, this pattern suggests an intense internal dynamical  
380 adjustment process. In comparison, LLJ\_non-HR events lacked such low-level  
381 momentum transfer signals (Fig. S7b and d) and maintained a quasi-steady state, with  
382 consistent LLJs strength (near  $11.8 \text{ m s}^{-1}$ ) and a preferred height range of 1–2 km AGL  
383 (Fig. 8f). The LLJs frequency exhibited gradual changes, peaking weakly at 36 min  
384 preceding rainfall before a subsequent rapid decrease (Fig. 7f). This pattern indicates

385 an absence of the rapid dynamical redistribution observed in LLJ\_non-HR events.

386 During Phase 3 in ROI-3, LLJ\_HR events exhibited a bimodal temporal  
387 distribution in LLJ frequency, with prominent peaks at  $-96$  min and  $-48$  min (Fig. 7c).  
388 The dominant LLJ height was centered between  $1$ – $1.5$  km AGL. The wind profiles  
389 showed a corresponding evolution where the maximum wind speed increased from  
390 approximately  $8.0$  m s $^{-1}$  at  $-120$  min to a first peak about  $9.5$  m s $^{-1}$  by  $-84$  min.  
391 Following a transient weakening ( $-48$  to  $-24$  min), a secondary intensification occurred  
392 immediately preceding HR onset (Fig. 8c). Conversely, LLJ\_non-HR events were  
393 characterized by substantially lower LLJs frequency (around 20%) and a more diffuse  
394 structure (Fig. 7g), with wind profiles exhibiting weaker intensification preceding  
395 rainfall (Fig. 8g). Consequently, the rapid reorganization and final intensification of  
396 LLJs appeared to be critical dynamical drivers for HR. However, despite the potential  
397 influences of regional thermodynamics and topography, the insufficient dynamical  
398 forcing from overall weaker wind profiles in ROI-3 remained the primary reason for its  
399 comparatively lower probability of heavier rainfall ( $\geq 2.0$  mm/6 min).

400 During Phase 4 in ROI-4, LLJ\_HR events exhibited a distinctive two-stage  
401 intensification process. The wind profiles initially strengthened rapidly starting from -  
402  $120$  min, reaching a primary peak of approximately  $12.8$  m s $^{-1}$  at  $-72$  min (Fig. 8d),  
403 coinciding with a secondary peak in LLJ frequency. Following a brief weakening ( $-60$   
404 to  $-48$  min), a renewed and explosive intensification occurred from  $-48$  min onwards,  
405 continuing until rainfall onset. Throughout this period, the LLJ cores remained  
406 concentrated between  $0.5$ – $1.5$  km AGL (Fig. 7d). In sharp contrast, LLJ\_non-HR  
407 events displayed a pattern of premature peaking followed by decay. Both frequency and  
408 intensity peaked earlier at  $-84$  min, followed by general attenuation (Fig. 7h). By  $-48$   
409 min, weakened wind profiles stabilized into a double-core structure maintaining around  
410  $10$  m s $^{-1}$ , with distinct jet cores near  $0.8$  km and  $1.7$  km AGL (Fig. 8h). Crucially, in  
411 the LLJ\_non-HR event, this premature peak and the subsequent continuous attenuation  
412 of the low-level wind field resulted in a lack of sustained dynamic forcing during the  
413 critical pre-rainstorm stage, failing to trigger HR.

414         Synthesizing the evolution across all phases, although a distinct transient  
415         weakening of the jet profile was consistently observed, LLJs exhibited a rapid re-  
416         intensification of wind speed accompanied by a lowering of the jet core height during  
417         approximately the final 30 min preceding HR. This recurring pre-rainfall adjustment  
418         suggests that LLJs underwent a short-term dynamical reorganization prior to HR onset.  
419         We propose that this minute-scale oscillatory behavior—characterized by a  
420         'weakening-then-strengthening' or 'descent-then-ascent' pattern—constitutes a robust  
421         dynamic precursor of HR. Physically, the temporary weakening may reflect momentum  
422         redistribution or enhanced turbulent mixing, whereas the subsequent intensification and  
423         descent of the jet core likely enhance low-level moisture convergence and vertical wind  
424         shear, thereby strengthening upward motion and promoting convective development  
425         (Markowski & Richardson, 2010). Such rapid structural adjustment indicates that the  
426         timing and vertical evolution of LLJs, rather than their mere presence, play a critical  
427         role in modulating heavy rainfall production.

428         Furthermore, probability distributions of LLJ strength and height within 2 hours  
429         preceding rainfall were compared across key regions (Fig. 9). During Phase 1 in ROI-  
430         1, the strength of LLJs in LLJ\_HR events was notably stronger by 2–3  $\text{m s}^{-1}$  than that  
431         in LLJ\_non-HR events (Fig. 9a). Height distributions showed distinct bimodal peaks  
432         near 0.9 km and 1.75 km AGL (Fig. 9e). The average LLJs height was generally higher  
433         in LLJ\_HR events, which is usually affected by the coupling of the upper-level jet  
434         stream or the land-sea breeze. During Phase 2 in ROI-2, LLJ\_HR events showed higher  
435         probabilities of strong LLJs (17–28  $\text{m s}^{-1}$ ) compared to the dominant 13  $\text{m s}^{-1}$  intensity  
436         in LLJ\_non-HR events (Fig. 9b). Influenced by large-scale circulation patterns, both  
437         event types featured LLJs centered near 1.5 km AGL (Fig. 9f), though LLJ\_HR events  
438         developed a secondary maximum near 0.8 km AGL due to pre-rainfall descent of the  
439         jet core (Fig. 7b). Contrastingly, Figure 9c shows that LLJ\_HR events were associated  
440         with weaker jet strengths (around 11  $\text{m s}^{-1}$ ) compared to LLJ\_non-HR events (14–23  
441          $\text{m s}^{-1}$ ) in ROI-3 during Phase 3, suggesting that strong LLJs don't necessarily induce  
442         HR here. The height of LLJ in LLJ\_HR events mainly concentrated near 1.2 km AGL,  
443         whereas in LLJ\_non-HR events, it was more uniformly distributed between 0–3 km

444 AGL with a higher probability nearly 1.5 km (Fig. 9g). For Phase 4 in ROI-4, LLJs  
445 strength peaked near  $15 \text{ m s}^{-1}$  in both event types, but LLJ\_HR events featured stronger  
446 jets reaching  $25\text{--}30 \text{ m s}^{-1}$  (Fig. 9d). The LLJs height in both events peaked  
447 predominantly at 0.8 km AGL, with secondary peaks at 1.5 km for LLJ\_HR and 2.0 km  
448 AGL for LLJ\_non-HR events (Fig. 9h).

449 In summary, although different internal dynamic adjustments, including frequency,  
450 occurrence height, and wind profile intensity of LLJs, preceding LLJ\_HR events were  
451 observed due to the different dominant mechanisms influencing rainfall in each phase,  
452 our findings highlight the role of fine-scale LLJ structures and their rapid vertical  
453 reorganization in modulating nocturnal rainfall intensity, offering valuable insights for  
454 improving regional nocturnal HR forecasting.

### 455 *3.3 Thermodynamic evolution associated with LLJs preceding nocturnal heavy* 456 *and non-heavy Rainfall*

457 The section 3.2 has clarified that the fine-scale dynamic characteristics of LLJs—  
458 including their temporal evolution, vertical structure and intensity variations—play a  
459 pivotal role in modulating nocturnal rainfall intensity during rainy season phases.  
460 However, the influence of LLJs on rainfall generation and intensification rarely  
461 operates in isolation; instead, it depends strongly on the accompanying large-scale  
462 thermodynamic environment, which provides the necessary moisture supply and  
463 convective instability to sustain or amplify heavy rainfall. Thus, to fully unravel the  
464 mechanisms underlying the distinction between LLJ\_HR and LLJ\_non-HR events, it is  
465 essential to complement the dynamic analysis with an in-depth examination of the  
466 thermodynamic conditions associated with LLJs within the immediate pre-convective  
467 environment (within 1-hour preceding rainfall).

468 Further analysis of the large-scale thermodynamic conditions at 1 hour prior to  
469 rainfall onset (Figs. 10 and 11) reveals consistently stronger thermal instability for  
470 LLJ\_HR versus LLJ\_non-HR events, accompanied by stronger MFC within key  
471 regions during each rainy season.

472 During Phase 1 in ROI-1, thermodynamic conditions were comparable between  
473 event types. Southwesterly LLJs transported warm-moist air masses from the South  
474 China Sea and Bay of Bengal, forming a pronounced warm-humid tongue (Fig. 10a and  
475 10e). Coupled with MFC centers developing north of the jet axis (Fig. 11a and 11e),  
476 this configuration facilitated nocturnal rainfall development. During Phase 2 in ROI-2,  
477 LLJ\_HR events exhibited a significantly stronger warm-moisture tongue with core  $\theta_e$   
478 reaching 358 K—approximately 2 K higher than in non-HR events (Figs. 10b and 10f).  
479 Dynamically, the stronger LLJ core (difference  $>1.2 \text{ m s}^{-1}$ ) drove a sharper, continuous  
480 band of MFC along the left flank of the jet axis (Fig. 11b), creating a robust triggering  
481 mechanism for HR (Fig. 11b). During Phase 3 in ROI-3, intensified southwesterly LLJs  
482 in HR events drove substantial northward transport of abundant moisture and higher  $\theta_e$   
483 air (difference  $>2 \text{ K}$ ) northward into a low  $\theta_e$  environment (Fig. 10c), enhancing  
484 convective instability. The synergistic interaction of this moist, high-energy advection  
485 with orographic forcing from the Taihang Mountains generated intense MFC, with peak  
486 values south of Beijing approximately  $30 \times 10^{-5} \text{ km m}^{-2} \text{ s}^{-1}$  (Fig. 11c) larger than those  
487 in LLJ\_non-HR events, thereby driving nocturnal HR. Thermodynamic contrasts were  
488 most pronounced during Phase 4 in ROI-4. Thermodynamic contrasts were most  
489 pronounced during Phase 4 in ROI-4. LLJ\_HR events featured a deep high- $\theta_e$  region  
490 ( $>356 \text{ K}$ ) over the southeastern Tibetan Plateau (Fig. 10d), contrasting with the cold  
491 highs located to the northeast of ROI-4 and lower  $\theta_e$  prevalent in LLJ\_non-HR events  
492 (Fig. 10h). Concurrently, accelerated easterly-southeasterly LLJs drove warm, moist air  
493 towards the steep eastern Plateau margin. The impingement of this flow against the  
494 sharp topographic gradient generated intense dynamic lifting and low-level  
495 convergence. This mechanically forced ascent, synergizing with the abundant moisture  
496 transport and strong MFC (Fig. 11h), played an essential role in triggering the observed  
497 nocturnal HR in this region.

498 To elucidate the rapid processes leading to occurrence of rainfall, the minute-scale  
499 evolution of key thermodynamic and dynamic parameters was further analyzed (Fig.  
500 12), including surface  $\theta_e$ , LLJ index and VWS. Specifically, LLJ index is defined as the  
501 ratio of maximum wind speed below 3 km to the height where wind first exceeds 10 m

502  $s^{-1}$ . A rapid rise in LLJ index will reflect the extension and pulsing intensity of the LLJ,  
503 and its magnitude has been shown to be positively correlated with subsequent rainfall  
504 intensity 1–2 hour later (Liu et al., 2003). VWS is calculated as the wind speed  
505 difference between the surface and jet height divided by the jet height and is used to  
506 characterize the bulk shear from the surface to the jet layer associated with the  
507 dynamical forcing and organization of convection (Wei et al., 2014).

508 Figure 12a illustrated that during Phase 1 in ROI-1, despite the similarity in large-  
509 scale environments between LLJ\_HR and LLJ\_non-HR events, they exhibited distinct  
510 differences in the continuous evolution of LLJ-associated thermodynamic conditions  
511 preceding rainfall onset. LLJ\_HR events exhibited abrupt thermodynamic enhancement  
512 from 90 min preceding the onset of rainfall driven by rapid intensification of LLJs, with  
513 surface  $\theta_e$  and VWS surging approximately 1.5 K and  $0.005 s^{-1}$  respectively.  
514 Concurrently, the LLJ index surged from approximately 0.05 to 0.08 and VWS peaked  
515 sharply at –60 min, signaling LLJs intensification and core descent (Figs. 7a, 8a). This  
516 rapid, minute-scale co-intensification of thermodynamic and dynamic processes serves  
517 as a critical precursor triggering HR. In contrast, LLJ\_non-HR events showed weaker  
518 increases of  $\theta_e$  and VWS and a declining LLJ index (by about 0.02) alongside rising jet  
519 cores, reducing low-level shear and convergence efficiency, thereby diminishing  
520 overall rainfall intensity.

521 During Phase 2 in ROI-2, the thermodynamic environment displayed a distinct  
522 ‘weakening-reintensification’ pattern (Fig. 12b), which aligns precisely with the  
523 intrinsic dynamical adjustments of the wind field presented in Fig. 8b. Initially, at -120  
524 min, concurrent peaks in the LLJ index and VWS were observed, coupled with a high  
525 surface  $\theta_e$  of 348.3 K. During the subsequent transition period, a drastic elevation in the  
526 jet core height starting from -84 min caused a precipitous drop in the LLJ index. The  
527 timing of this rapid evolution suggests a transient optimal window for nocturnal rainfall  
528 triggering that is characteristic of LLJ\_HR events in ROI-2. Following this, rapid  
529 surface cooling began 60 min prior to HR. This cooling was likely induced by the cold  
530 pool outflows associated with alternation or propagation of convective systems  
531 embedded within the Mei-Yu front cloud system (Zhang et al., 2023). The resulting

532 dense cold air wedging beneath the strong southwesterly LLJs can lift the jet axis above  
533 the cold-pool interface, further enhancing uplift and promoting rainfall (Luo et al.,  
534 2014). This in turn facilitated the final re-intensification of the jet structure (Fig. 7b and  
535 8b). Crucially, this reorganized configuration sharply enhances low-level vertical wind  
536 shear and horizontal convergence (Fig. 12b), further promoting HR development. In  
537 contrast, LLJ\_non-HR events exhibited weaker thermodynamic support and diminished  
538 dynamic forcing with consistently lower LLJ indices within 60 min preceding rainfall,  
539 resulting in insufficient lift to sustain HR. Compared with the disordered fluctuations  
540 of the LLJ\_non-HR events, LLJ\_HR events highlight the importance of thermal-  
541 dynamic synergy influenced by LLJs evolution. Even though the LLJ evolution may be  
542 modulated by convective feedback, the resulting reorganized jet profile still can serve  
543 as a robust dynamical precursor essential for triggering local HR.

544 During Phase 3 in ROI-3, LLJ\_HR events featured prominent thermal  
545 compensation (surface  $\Delta\theta_e > 1\text{K}$ , 850hPa  $\Delta\theta_e > 2\text{K}$  versus non-HR events)—despite  
546 possessing generally weaker dynamical forcing compared to other phases (Fig. 12c).  
547 Temporally, the evolution was marked by distinct pulsations: The LLJ index exhibited  
548 a rapid rise (from  $\sim 0.03$  to  $\sim 0.06$ ) starting 84 min prior to HR onset (Fig. 12c) driven  
549 by a surge of LLJs profiles, while VWS peaked synchronously with the maximum LLJ  
550 frequency. Subsequently, a secondary peak in both the LLJ index and VWS was  
551 observed between  $-60$  and  $-48$  min. Although the subsequent declines in wind speed  
552 and frequency led to notable fluctuations in these parameters, the VWS and LLJ index  
553 underwent substantial intensification (with VWS increasing by  $\sim 1.5\text{ s}^{-1}$ ) in the final 24  
554 min, driven by the rapid acceleration of the LLJ wind field. This co-evolution with rapid  
555 surface warming (increase of  $0.25\text{ K}$ ) released convective instability and enhanced  
556 convergence (Fig. 10). Nevertheless, the overall weaker dynamical conditions likely  
557 limited the depth and organization of convection, potentially accounting for the reduced  
558 probability of heavier rainfall compared to other phases. In contrast, during LLJ non-  
559 HR events, the LLJ index ( $\sim 0.03$ ) and  $\theta_e$  vary rather gradually.

560 During Phase 4 in ROI-4, under the favorably thermal environments ( $\theta_e > 346\text{ K}$ ),  
561 LLJ\_HR events showed a two-stage dynamic intensification. Initially, the LLJ index

562 surged, while the VWS and jet intensity reached synchronous secondary peaks at  $-72$   
563 min. In the second stage, VWS increased rapidly by  $\sim 0.9$  (Fig. 12d), and the LLJ index  
564 maintained an overall upward trend, peaking immediately prior to onset due to the  
565 surging jet. But LLJ\_non-HR events showed weakening trends in both dynamic and  
566 thermodynamic conditions during the final 30 min and exhibited weaker changes  
567 ( $\Delta VWS < 0.45 \text{ s}^{-1}$ ,  $\Delta \text{LLJ index} < 0.02$ ), reflecting an absence of the coordinated  
568 intensification necessary to initiate and sustain HR.

569 Although the evolution paths of the thermodynamic environment vary across  
570 different phases, a universal cross-region precursor emerges: the LLJ index and VWS  
571 consistently exhibits a strengthening or stabilizing trend in the final approximately 30  
572 min preceding HR onset, operating in concert with significant low-level warming  
573 (rising  $\theta_e$ ). In contrast, non-HR events generally lack this culminating dynamical  
574 intensification. Overall, these results adequately showcase the sensitivity of regional  
575 HR to the fine-scale structural evolution of LLJs and their coupling with  
576 thermodynamic environments.

#### 577 **4. Summary and concluding remarks**

578 Using wind profile measurements from a nationwide network of 31 RWPs during  
579 the warm seasons (April–October) of 2023–2024, this study characterized the minute-  
580 scale evolution of LLJs as dynamic precursors to nocturnal rainfall across China. By  
581 systematically comparing the vertically resolved structure and temporal evolution of  
582 LLJs within the 2-hour window preceding nocturnal HR and non-HR events across four  
583 distinct rainy-season phases, we identified the key dynamic-thermodynamic  
584 distinctions governing rainfall intensity.

585 At the national scale, nocturnal rainfall accounted for nearly half of the total warm-  
586 season precipitation, and 56% of nocturnal rainfall events were preceded by LLJs  
587 within 2 hours. In the key regions of interest (ROIs), approximately 45.0% of identified  
588 HR events were associated with LLJs. Overall, LLJ-related events were significantly  
589 more prone to producing heavier rainfall than non-LLJ events across most regions,  
590 underscoring the strong coupling between LLJs and nocturnal HR.

591 Despite regional differences in synoptic forcing, consistent contrast in LLJ  
592 evolution were observed between HR and non-HR events across all phases. During  
593 Phase 1 in ROI-1, a bimodal vertical distribution of LLJs and their rapid  
594 thermodynamic-dynamic co-intensification starting 84 min prior to rainfall were  
595 identified as key precursors of LLJ\_HR events, in sharp contrast to the decoupled  
596 dynamics of LLJ\_non-HR events. Phase 2 (ROI-2) was characterized by a distinct  
597 oscillatory process, where HR events featured a rapid descent of the LLJ core below 1  
598 km followed by a robust rebound, distinguishing them from the quasi-steady state of  
599 LLJ\_non-HR cases. In Phase 3 (ROI-3), LLJ\_HR events exhibited significant thermal  
600 compensation and bimodal pulsations (peaks at  $-96$  and  $-48$  min), with a critical final-  
601 stage intensification serving as the decisive trigger. Similarly, Phase 4 (ROI-4) featured  
602 a distinctive two-stage intensification, where a rapid LLJ surge within 48 min of onset  
603 distinguished LLJ\_HR events from the significantly attenuated dynamical structures of  
604 LLJ\_non-HR events.

605 Although the detailed dynamical pathways vary among phases, a unifying feature  
606 emerges: all LLJ\_HR events exhibit a ‘final-stage intensification’ of low-level  
607 dynamics—manifested as enhanced LLJ strength, vertical wind shear, and LLJ index—  
608 within approximately 30 min preceding rainfall, occurring in synergy with increasing  
609 thermodynamic instability (e.g., rising equivalent potential temperature,  $\theta_e$ ). This result  
610 confirms the universality of the final-stage low-level dynamic amplification identified  
611 in our previous study (Li et al., 2024) and demonstrates its national-scale applicability  
612 across diverse monsoon regimes.

613 Crucially, this study further identifies a previously under-resolved “preparatory  
614 adjustment” phase occurring 30–120 minutes prior to rainfall onset, during which LLJ  
615 frequency, strength and core height undergo systematic minute-scale reorganization.  
616 This national-scale evidence indicates that the final dynamic trigger is contingent upon  
617 this earlier synergistic coupling of minute-scale jet structural evolution and  
618 thermodynamic destabilization. This rapid, synergistic reorganization represents a  
619 necessary precondition for HR generation and contrasts sharply with the comparatively  
620 steady evolution observed in LLJ\_non-HR events. These results highlight that the

621 occurrence and intensity of nocturnal rainfall are governed not simply by LLJ presence,  
622 but by the fine-scale vertical evolution of LLJs and their interaction with regional  
623 thermodynamic conditions.

624 Overall, this study establishes robust dynamic-rainfall linkages associated with  
625 LLJs across different warm-season rainy periods in China. Future research should: (1)  
626 expand multi-source observations to establish dynamic thresholds for early forecasting  
627 systems of nocturnal rainfall, and (2) develop quantitative frameworks relating LLJ  
628 structural evolution to rainfall intensity, offering theoretical support for optimizing  
629 physical processes in LLJ parameterization schemes within high-resolution numerical  
630 models. Further investigation is also needed to clarify the physical mechanisms  
631 controlling rapid adjustments in LLJ core height and strength immediately prior to  
632 rainfall onset.

### 633 **Data Availability**

634 The LLJs retrieved from the RWP network can be acquired from  
635 <https://doi.org/10.5281/zenodo.17176759> (Li and Guo, 2025). The data from the  
636 weather station are obtained from the China Meteorological Data Service Centre at  
637 <https://data.cma.cn/en>, and the original ERA5 reanalysis data used here are available  
638 from the ECMWF in Hersbach et al. (2020).

### 639 **Acknowledgments**

640 This work was supported by the National Natural Science Foundation of China  
641 under grant 42325501, the Science and Technology Supporting Project of Guizhou  
642 Province ([2023]236) and the National Key Research and Development Program of  
643 China under grant 2024YFC3013001. Last but not least, we appreciated tremendously  
644 the constructive comments and suggestions made by the anonymous reviewers that  
645 significantly improved the quality of our manuscript.

### 646 **Author Contributions**

647 The study was completed with close cooperation between all authors. JG designed  
648 the research framework; NL performed the analysis and drafted the original manuscript

649 with contribution from JG; JG, XG, ZZ, YZ. JG, NT, YW, and YZ helped revise the  
650 manuscript.

651 **Completing interests**

652 The authors declare that they have no conflict of interest.

653

654 **References**

- 655 Anthes, R. A., Kuo, Y. H., Benjamin, S. G., and Li, Y. F: The evolution of the mesoscale  
656 environment of severe local storms: Preliminary modeling results, *Mon. Weather*  
657 *Rev.*, 110(9), 1187-1213, doi:10.1175/1520-0493(1982)110,1187:  
658 TEOTME.2.0.CO;2, 1982.
- 659 Bai, L., Chen, G., Huang, Y., and Meng, Z.: Convection initiation at a coastal rainfall  
660 hotspot in South China: Synoptic patterns and orographic effects, *J. Geophys. Res.*  
661 *Atmos.*, 126(24), e2021JD034642, doi: 10.1029/2021JD034642, 2021.
- 662 Blackadar, A. K.: Boundary layer wind maxima and their significance for the growth  
663 of nocturnal inversions, *Bull. Am. Meteorol. Soc.*, 38(5), 283-290,  
664 doi:10.1175/1520-0477-38.5.283, 1957.
- 665 Bonner, W. D.: Climatology of the low-level jet, *Mon. Weather Rev.*, 96(12), 833-850.  
666 doi:10.1175/1520-0493(1968)096<0833:COTLLJ>2.0.CO;2, 1968.
- 667 Cao, Q., J. Guo, C. Xue, Z. Li, H. Xu, N. Li, Y. Sun, Z. Zhang, Y. Wang, J. Chen, Y.  
668 Zhou, and T. Chen: Divergent Sounding-derived Precursor Pathways Enable  
669 Discrimination of Dry versus Wet Severe Convective Winds. *Geophysical*  
670 *Research Letters*, 52, e2025GL117491. <https://doi.org/10.1029/2025GL117491>,  
671 2025.
- 672 Carbone, R. E., and Tuttle, J. D.: Rainfall occurrence in the US warm season: The  
673 diurnal cycle, *J. Clim.*, 21(16), 4132-4146, doi:10.1175/2008JCLI2275.1, 2008.
- 674 Chen, G., Sha, W., Iwasaki, T., and Wen, Z.: Diurnal Cycle of a Heavy Rainfall  
675 Corridor over East Asia, *Mon. Weather Rev.*, 145(8), 3365-3389,  
676 doi:10.1175/mwr-d-16-0423.1, 2017.
- 677 Chen, H., Zhou, T., Neale, R. B., Wu, X., and Zhang, G. J.: Performance of the new  
678 NCAR CAM3. 5 in East Asian summer monsoon simulations: Sensitivity to  
679 modifications of the convection scheme, *J. Clim.*, 23(13), 3657-3675,  
680 doi:10.1175/2010JCLI3022.1, 2010.
- 681 Chen, T., Guo, J., Guo, X., Zhang, Y., Xu, H., and Zhang, D.-L.: On the multiscale  
682 processes leading to an extreme gust wind event in East China: Insights from radar

683 wind profiler mesonet observations. *Journal of Geophysical Research:*  
684 *Atmosphere*, 129, e2024JD041484, [doi: 10.1029/2024JD041484](https://doi.org/10.1029/2024JD041484), 2024.

685 Chen, X., F. Zhang, and K. Zhao: Diurnal Variations of the Land-Sea Breeze and Its  
686 Related Precipitation over South China. *J. Atmos. Sci.*, 73, 4793 - 4815,  
687 [doi:10.1175/JAS-D-16-0106.1](https://doi.org/10.1175/JAS-D-16-0106.1), 2016.

688 Chen, Y. L., and Li, J.: Large-scale conditions favorable for the development of heavy  
689 rainfall during TAMEX IOP 3, *Mon. Weather Rev.*, 123(10), 2978-3002, 1995.

690 China Meteorological Administration: Specification for Automatic Observation of  
691 Ground Meteorology. China Meteorological Press, 2020.

692 Davis, C. A., Maning, W. K., Carbone, R., Trier, S., and Tuttle, J.: Coherence of warm-  
693 season continental rainfall in numerical weather prediction models, *Mon. Weather*  
694 *Rev.*, 131, 2667-2679, [doi:10.1175/1520-](https://doi.org/10.1175/1520-0493(2003)131<2667:COWCRI>2.0.CO;2)  
695 [0493\(2003\)131<2667:COWCRI>2.0.CO;2](https://doi.org/10.1175/1520-0493(2003)131<2667:COWCRI>2.0.CO;2), 2003.

696 Dong, F., Zhi, X., Zhang, L., and Ye, C.: Diurnal variations of coastal boundary layer  
697 jets over the northern South China Sea and their impacts on diurnal cycle of  
698 rainfall over southern China during the early-summer rainy season, *Mon. Weather*  
699 *Rev.*, 149(10), 3341-3363, [doi:10.1175/MWR-D-20-0292.1](https://doi.org/10.1175/MWR-D-20-0292.1), 2021.

700 Doubler, D. L., Winkler, J. A., Bian, X., Walters, C. K., and Zhong, S.: An NARR-  
701 derived climatology of southerly and northerly low-level jets over North America  
702 and coastal environs, *J. Appl. Meteorol. Climatol.*, 54(7), 1596-1619,  
703 [doi:10.1175/JAMC-D-14-0311.1](https://doi.org/10.1175/JAMC-D-14-0311.1), 2015.

704 Du, Y., and Chen, G.: Heavy Rainfall Associated with Double Low-Level Jets over  
705 Southern China. Part II: Convection Initiation, *Mon. Weather Rev.*, 147(2), 543-  
706 565, [doi:10.1175/mwr-d-18-0102.1](https://doi.org/10.1175/mwr-d-18-0102.1), 2019.

707 Du, Y., and G. Chen: Heavy Rainfall Associated with Double Low-Level Jets over  
708 Southern China. Part I: Ensemble-Based Analysis, *Monthly Weather Review*, 146,  
709 3827 - 3844, [doi: 10.1175/MWR-D-18-0101.1](https://doi.org/10.1175/MWR-D-18-0101.1), 2018.

710 Du, Y., Chen, G., Han, B., Bai, L., and Li, M.: Convection initiation and growth at the  
711 coast of South China. Part II: Effects of the terrain, coastline, and cold pools, *Mon.*  
712 *Weather Rev.*, 148(9), 3871-3892, [doi:10.1175/MWR-D-20-0090.1](https://doi.org/10.1175/MWR-D-20-0090.1), 2020.

713 Du, Y., Zhang, Q., Ying, Y., and Yang, Y.: (2012). Characteristics of low-level jets in  
714 Shanghai during the 2008-2009 warm seasons as inferred from wind profiler radar  
715 data, *J. Meteorol. Soc. Jpn. Ser. II*, 90(6), 891-903, doi:10.2151/jmsj.2012-603,  
716 2012.

717 Fu, S. M., Jin, S. L., Shen, W., Li, D. Y., Liu, B., & Sun, J. H.: A kinetic energy budget  
718 on the severe wind production that causes a serious state grid failure in Southern  
719 Xinjiang China, *Atmospheric Science Letters*, 21(7), e977, 2020.

720 Gebauer, J. G., Shapiro, A., Fedorovich, E., and Klein, P.: (2018). Convection Initiation  
721 Caused by Heterogeneous Low-Level Jets over the Great Plains, *Mon. Weather*  
722 *Rev.*, 146(8), 2615-2637, doi:10.1175/mwr-d-18-0002.1, 2018.

723 Guo, J., Liu, B., Gong, W., Shi, L., Zhang, Y., Ma, Y., Zhang, J., Chen, T., Bai, K.,  
724 Stoffelen, A., de Leeuw, G., and Xu, X.: Technical note: First comparison of wind  
725 observations from ESA's satellite mission Aeolus and ground-based radar wind  
726 profiler network of China, *Atmos. Chem. Phys.*, 21, 2945-2958, doi: 10.5194/acp-  
727 21-2945-2021, 2021 (data available at: <https://data.cma.cn>, last access: 11 January  
728 2024).

729 Guo, X., Guo, J., Chen, T., Li, N., Zhang, F., and Sun, Y.: Revisiting the evolution of  
730 downhill thunderstorms over Beijing: a new perspective from a radar wind profiler  
731 mesonet, *Atmos. Chem. Phys.*, 24(14), 8067-8083, doi:10.5194/acp-24-8067-  
732 2024, 2024.

733 Guo, X., Guo, J., Zhang, D. L., and Yun, Y.: Vertical divergence profiles as detected  
734 by two wind-profiler mesonets over East China: Implications for nowcasting  
735 convective storms, *Q. J. R. Meteorol. Soc.*, 149(754), 1629-1649.  
736 doi:10.1002/qj.4474, 2023.

737 Hersbach, H., Bell, B., Berrisford, P., Biavati, G., Horányi, A., Muñoz Sabater, J.,  
738 Nicolas, J., Peubey, C., Radu, R., Rozum, I., Schepers, D., Simmons, A., Soci, C.,  
739 Dee, D. and Thépaut, J-N.: ERA5 hourly data on pressure levels from 1940 to  
740 present. Copernicus Climate Change Service (C3S) Climate Data Store (CDS),  
741 doi: 10.24381/cds.bd0915c6 (Accessed on 06-05-2024), 2023.

742 Higgins, R. W., Yao, Y., Yarosh, E. S., Janowiak, J. E., and Mo, K. C.: Influence of the  
743 Great Plains low-level jet on summertime precipitation and moisture transport  
744 over the central United States, *J. Clim.*, 10(3), 481-507, 1997.

745 Hodges, D., and Pu, Z.: Characteristics and Variations of Low-Level Jets and  
746 Environmental Factors Associated with Summer Precipitation Extremes over the  
747 Great Plains. *J. Clim.*, 32(16), 5123-5144, doi:10.1175/JCLI-D-18-0553.1, 2019.

748 Holton, J. R.: The diurnal boundary layer wind oscillation above sloping terrain, *Tellus*,  
749 19(2), 200-205, doi: 10.3402/tellusa.v19i2.9766, 1967.

750 Horinouchi, T., Matsumura, S., Ose, T., and Takayabu, Y. N.: Jet-precipitation relation  
751 and future change of the mei-yu-baiu rainband and subtropical jet in CMIP5  
752 coupled GCM simulations, *J. Clim.*, 32(8), 2247-2259, doi:10.1175/JCLI-D-18-  
753 0426.1, 2019.

754 Huang, X., Sun, J., and Liu, W.: The interaction between low-level jet evolution and  
755 severe convective rainstorms under topographic effect, *Acta Meteorol. Sin.*, 78(4),  
756 551-567, 2020.

757 Li, N., and Guo, J.: Data for wind profiles associated with LLJs obtained from RWP  
758 observations during the warm season (April-October) of 2023-2024 in China [Data  
759 set]. Zenodo. <https://doi.org/10.5281/zenodo.17176759>, 2025.

760 Li, N., Guo, J., Wu, M., Zhang, F., Guo, X., Sun, Y., Zhang Z., Liang L., Chen T.: Low-  
761 level jet and its effect on the onset of summertime nocturnal rainfall in Beijing,  
762 *Geophys. Res. Lett.*, 51, e2024GL110840, doi:10.1029/2024GL11084, 2024.

763 Li, X., and Du, Y.: Statistical relationships between two types of heavy rainfall and  
764 low-level jets in South China, *J. Clim.*, 34(21), 8549-8566, doi:10.1175/JCLI-D-  
765 21-0121.1, 2021.

766 Liu, B., Ma, Y., Guo, J. and Wei, G.: Boundary layer heights as derived from ground-  
767 based radar wind profiler in Beijing, *IEEE Trans. Geosci. Remote Sens.*, 57, 8095-  
768 8104, doi:10.1109/TGRS.2019.2918301, 2019.

769 Liu, X., Luo, Y., Huang, L., Zhang, D. L., & Guan, Z: Roles of double low-level jets in  
770 the generation of coexisting inland and coastal heavy rainfall over south China

771 during the presummer rainy season, *Journal of Geophysical Research:*  
772 *Atmospheres*, 125(18), e2020JD032890, 2020.

773 Luo, Y., Gong, Y., and Zhang, D. L.: Initiation and organizational modes of an extreme-  
774 rain-producing mesoscale convective system along a mei-yu front in East China,  
775 *Mon. Weather Rev.*, 142(1), 203-221, doi:10.1175/MWR-D-13-00111.1, 2014.

776 Maddox, R. A.: Large-scale meteorological conditions associated with midlatitude,  
777 mesoscale convective complexes, *Mon. Weather Rev.*, 111(7), 1475-1493, 1983.

778 Marengo, J. A., Soares, W. R., Saulo, C., and Nicolini, M.: Climatology of the low-  
779 level jet east of the Andes as derived from the NCEP-NCAR reanalyses:  
780 Characteristics and temporal variability, *J. Clim.*, 17(12), 2261-2280, 2004.

781 Markowski, P., & Richardson, Y.: *Mesoscale meteorology in midlatitudes*, John Wiley  
782 & Sons, 2011.

783 Miao, Y., Guo, J., Liu, S., Wei, W., Zhang, G., Lin, Y., and Zhai, P.: The Climatology  
784 of Low-Level Jet in Beijing and Guangzhou, China, *J. Geophys. Res. Atmos.*,  
785 123(5), 2816-2830. doi:10.1002/2017jd027321, 2018.

786 Mitchell, M. J., Arritt, R. W., and Labas, K.: A climatology of the warm season Great  
787 Plains low-level jet using wind profiler observations, *Weather Forecast.*, 10(3),  
788 576-591, 1995.

789 Molod, A., Salmun, H. and Collow, A.B.M.: Annual cycle of planetary boundary layer  
790 heights estimated from wind profiler network data, *J. Geophys. Res. Atmos.*, 124,  
791 6207-6221, doi:10.1029/2018JD030102, 2019.

792 Monaghan, A. J., Rife, D. L., Pinto, J. O., Davis, C. A., and Hannan, J. R.: Global  
793 precipitation extremes associated with diurnally varying low-level jets, *J. Clim.*,  
794 23(19), 5065-5084, 2010.

795 Pan, H., and Chen, G.: Diurnal variations of precipitation over North China regulated  
796 by the mountain-plains solenoid and boundary-layer inertial oscillation, *Adv.*  
797 *Atmos. Sci.*, 36(8), 863-884, doi:10.1175/2010JCLI3515.1, 2019.

798 Pitchford, K. L., and London, J.: The low-level jet as related to nocturnal thunderstorms  
799 over Midwest United States, *J. Appl. Meteorol.*, 1(1), 43-47, 1962.

800 Rasmussen, K. L., and Houze Jr, R. A.: Convective initiation near the Andes in  
801 subtropical South America, *Mon. Weather Rev.*, 144(6), 2351-2374,  
802 doi:10.1175/MWR-D-15-0058.1, 2016.

803 Reif, D. Q., and Bluestein, H.: A 20-year climatology of nocturnal convection initiation  
804 over the central and southern great plains during the warm season, *Mon. Weather*  
805 *Rev.*, 145, 1615-1639, doi:10.1175/MWR-D-16-0340.1, 2017.

806 Roots, M., Sullivan, J. T., and Demoz, B.: Mid-Atlantic nocturnal low-level jet  
807 characteristics: a machine learning analysis of radar wind profiles, *Atmos. Meas.*  
808 *Tech.*, 18(5), 1269-1282, doi:10.5194/amt-18-1269-2025, 2025.

809 Stensrud, D. J.: Importance of low-level jets to climate: A review, *J. Clim.*, 1698-1711,  
810 1996.

811 Subrahmayam, K. V., Udupa, S. R., Kumar, K. K., Ramana, M. V., Srinivasulu, J., and  
812 Bothale, R. V.: Prediction of zonal wind using machine learning algorithms:  
813 Implications to future projections of Indian monsoon jets, *J. Indian Soc. Remote*  
814 *Sens.*, 52(2), 371-381, 2024.

815 Sun, S. Q., Zhai, G. H., and Lorenzo, D. O.: The relationship between large-scale low-  
816 level jet over east asia and monsoon as well as cross-equatorial currents in  
817 summer, *Acta Meteorol. Sin.*, 1(1), 43-50, 1986.

818 Trier, J. W. Wilson, D. A. Ahijevych, and R. A. Sobash : Mesoscale vertical motions  
819 near nocturnal convection initiation in PECAN, *Mon. Weather Rev.*, 145, 2919-  
820 2941, doi:10.1175/MWR-D-17-0005.1, 2017.

821 Trier, S. B., Davis, C. A., Ahijevych, D. A., Weisman, M. L., and Bryan, G. H.:  
822 Mechanisms supporting long-lived episodes of propagating nocturnal convection  
823 within a 7-day WRF model simulation, *J. Atmos. Sci.*, 63(10), 2437-2461, doi:  
824 10.1175/JAS3768.1, 2006.

825 Tuttle, J. D., and Davis, C. A.: Corridors of warm season precipitation in the central  
826 United States. *Mon. Weather Rev.*, 134(9), 2297-2317, doi:10.1175/MWR3188.1,  
827 2006.

828 Uccellini, L. W., and D. R. Johnson: The coupling of upper and lower tropospheric jet  
829 streaks and implications for the development of severe convective storms.

830 Monthly Weather Review, 107, 682-703, doi: 10.1175/1520-  
831 0493(1979)107,0682:TCOUAL.2.0.CO;2, 1979.

832 Walters, C. K., Winkler, J. A., Shadbolt, R. P., van Ravensway, J., and Bierly, G. D.:  
833 A long-term climatology of southerly and northerly low-level jets for the central  
834 United States, *Ann. Assoc. Am. Geogr.*, 98(3), 521-552, 2008.

835 Wang, D., Zhang, Y., and Huang, A.: Climatic features of the south-westerly low-level  
836 jet over southeast China and its association with precipitation over east China,  
837 *Asia-Pac. J. Atmos. Sci.*, 49(3), 259-270, doi:10.1007/s13143-013-0025-y, 2013.

838 Wang, W. C., Gong, W., and Wei, H.: A regional model simulation of the 1991 severe  
839 precipitation event over the Yangtze-Huai River valley. Part I: Precipitation and  
840 circulation statistics, *J. Clim.*, 13(1), 74-92, doi:10.1175/1520-  
841 0442(2000)013<0074:ARMSOT>2.0.CO;2, 2000.

842 Weckwerth, T. M., and Wakimoto, R. M.: The initiation and organization of convective  
843 cells atop a cold-air outflow boundary, *Mon. Weather Rev.*, 120(10), 2169–2187,  
844 doi:10.1175/1520-0493(1992)120,2169:TIAOOC.2.0.CO;2, 1992.

845 Weckwerth, T. M., Hanesiak, J., Wilson, J. W., et al.: Nocturnal convection initiation  
846 during PECAN 2015, *Bull. Am. Meteorol. Soc.*, 100(11), 2223-2239,  
847 doi:10.1175/BAMS-D-18-0299.1, 2019.

848 Wei, W., Zhang, H. S., and Ye, X. X.: Comparison of low-level jets along the north  
849 coast of China in summer, *J. Geophys. Res. Atmos.*, 119(16), 9692-9706.  
850 doi:10.1002/2014jd021476, 2014.

851 Weisman, M. L., Trapp, R. J., Romine, G. S., Davis, C., Torn, R., Baldwin, M., Bosart,  
852 L., Brown, J., Coniglio, M., Dowell, D., Evans, A. C., Galarneau, T. J., Haggerty,  
853 J., Hock, T., Manning, K., Roebber, P., Romashkin, P., Schumacher, R., Schwartz,  
854 C. S., Sobash, R., Stensrud, D., and Trier, S. B.: The mesoscale predictability  
855 experiment (MPEX), *Bull. Am. Meteorol. Soc.*, 96(12), 2127-2149,  
856 doi:10.1175/bams-d-13-00281.1, 2015.

857 Whiteman, C. D., Bian, X., and Zhong, S.: Low-level jet climatology from enhanced  
858 Rawinsonde observations at a site in the southern Great Plains, *J. Appl. Meteorol.*,

859 36(10), 1363-1376, doi:10.1175/1520-  
860 0450(1997)036%3C1363:LLJCFE%3E2.0.CO;2, 1997.

861 Xia, R., and Zhao, S.: Diagnosis and modeling of meso-scale systems of heavy rainfall  
862 in warm sector ahead of front in South China (middle part of Guangdong province)  
863 in June 2005, *Chin. J. Atmos. Sci.*, 33(3), 2009.

864 Xue, M., Luo, X., Zhu, K., Sun, Z., and Fei, J.: The controlling role of boundary layer  
865 inertial oscillations in Meiyu frontal precipitation and its diurnal cycles over  
866 China, *J. Geophys. Res. Atmos.*, 123(10), 5090-5115,  
867 doi:10.1029/2018JD028368, 2018.

868 Yan, Y., Cai, X., Wang, X., Miao, Y., and Song, Y.: Low-level jet climatology of China  
869 derived from long-term radiosonde observations, *J. Geophys. Res. Atmos.*,  
870 126(20), e2021JD035323, doi:10.1029/2021JD035323, 2021.

871 Yu, R., Li, J., Chen, H., and Yuan, W.: Progress in studies of the precipitation diurnal  
872 variation over contiguous China, *J. Meteorol. Res.*, 28(5), 877-902,  
873 doi:10.1007/s13351-014-3272-7, 2014.

874 Zamora, R.J., Shapiro, M.A. and Doswell, C.A., III.: The diagnosis of upper  
875 tropospheric divergence and ageostrophic wind using profiler wind observations,  
876 *Mon. Weather Rev.*, 115, 871-884, doi:10.1175/1520-0493(1987)1152.0.CO;2,  
877 1987.

878 Zhang, F., Zhang, Q., Sun, J., and Xu, J.: Convection initiation during the Meiyu  
879 environment in the Yangtze-Huai River basin of China, *J. Geophys. Res. Atmos.*,  
880 128(9), e2022JD038077, doi:10.1029/2022JD038077, 2023.

881 Zhang, M., and Meng, Z.: Warm-sector heavy rainfall in southern China and its WRF  
882 simulation evaluation: A low-level-jet perspective, *Mon. Weather Rev.*, 147(12),  
883 4461-4480, doi:10.1175/MWR-D-19-0110.1, 2019.

884 Zhang, Y., Xue, M., Zhu, K., and Zhou, B.: What is the main cause of diurnal variation  
885 and nocturnal peak of summer precipitation in Sichuan Basin, China? the key role  
886 of boundary layer low-level jet inertial oscillations, *J. Geophys. Res. Atmos.*,  
887 124(5), 2643-2664, doi:10.1029/2018jd029834, 2019.

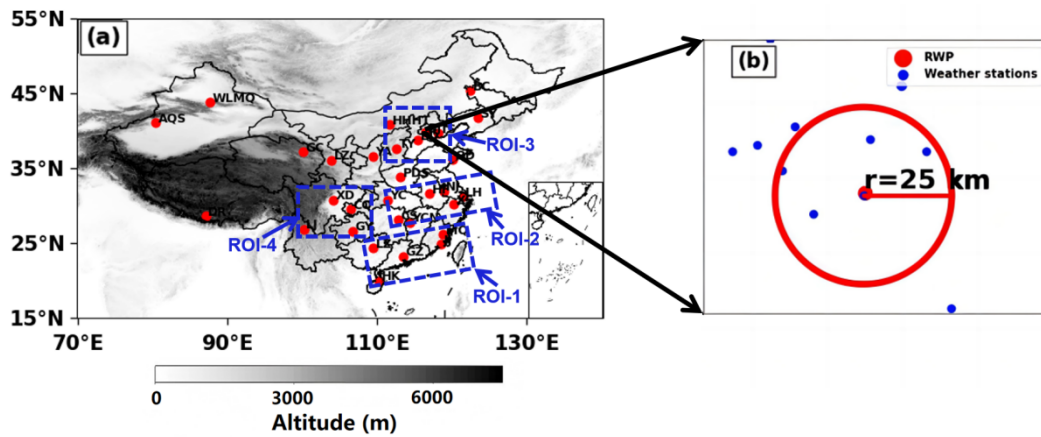
888 Zhao, Y., Liao, J., Zhang, Q., Chen, J., Gong, X., Shi, Y., Shi, M., Yang, D., Fan, S.,  
889 Zhou, X., Cao, L., and Hu, K.: Development of China Ground Climate Normal  
890 Value Dataset from 1991 to 2020, Chinese Journal of Atmospheric Sciences (in  
891 Chinese), 48(2), 555–571, doi:10.3878/j.issn.1006-9895.2204.22010, 2024.  
892  
893

Table 1. Table of Representative Radar Wind Profiler Stations in Mainland China

Region	Station	Longitude (°)	Latitude (°)	Altitude (m)	
ROI-1	58839	MQ	118.86	26.22	160.70
	59046	LZ	109.46	24.36	314.40
	59137	JJ	118.54	24.81	124.80
	59287	GZ	113.48	23.21	65.00
	59758	HK	110.25	19.99	69.00
ROI-2	57461	YC	111.36	30.74	253.80
	57687	CS	112.79	28.11	119.00
	57793	YCN	114.36	27.79	132.00
	58238	BJ	118.90	31.93	40.60
	58321	HF	117.03	31.57	50.00
	58367	LH	121.47	31.18	5.00
	58459	XS	120.29	30.18	48.80
ROI-3	53463	HHHT	111.68	40.82	1152.10
	53772	TY	112.58	37.62	785.00
	54511	BJ	116.47	39.81	31.50
	54534	TS	118.10	39.65	23.20
	54602	BD	115.48	38.73	16.80
ROI-4	57816	GY	106.73	26.59	1197.60
	56290	XD	104.18	30.77	514.00
	56651	LJ	100.22	26.85	2382.40
Other stations	50936	BC	122.47	45.36	156.00
	51463	WLMQ	87.65	43.79	935.00
	51628	AKS	80.38	41.12	1107.10
	52754	GC	100.08	37.2	3301.50
	52889	LZ	103.89	36.06	1519.20
	57516	CQ	106.46	29.57	260.00
	53845	YA	109.45	36.58	1180.40
	54342	SY	123.51	41.73	50.00
	54857	QD	120.13	36.23	12.00
	55664	DR	87.07	28.63	4302.00
	57171	PDS	113.12	33.77	142.00

895 Figures

896



897

898 Figure.1 (a) Spatial distribution of 31 Radar Wind Profiler (RWP) stations (red dots)  
899 across China, with four regions of interest (ROIs) demarcated by blue dashed boxes:  
900 ROI-1, ROI-2, ROI-3, and ROI-4. (b) Schematic of spatial co-location: Beijing  
901 Observatory's RWP (red circle) and rain gauges (blue dots) within a 25-km radius

902

903

904

905

906

907

908

909

910

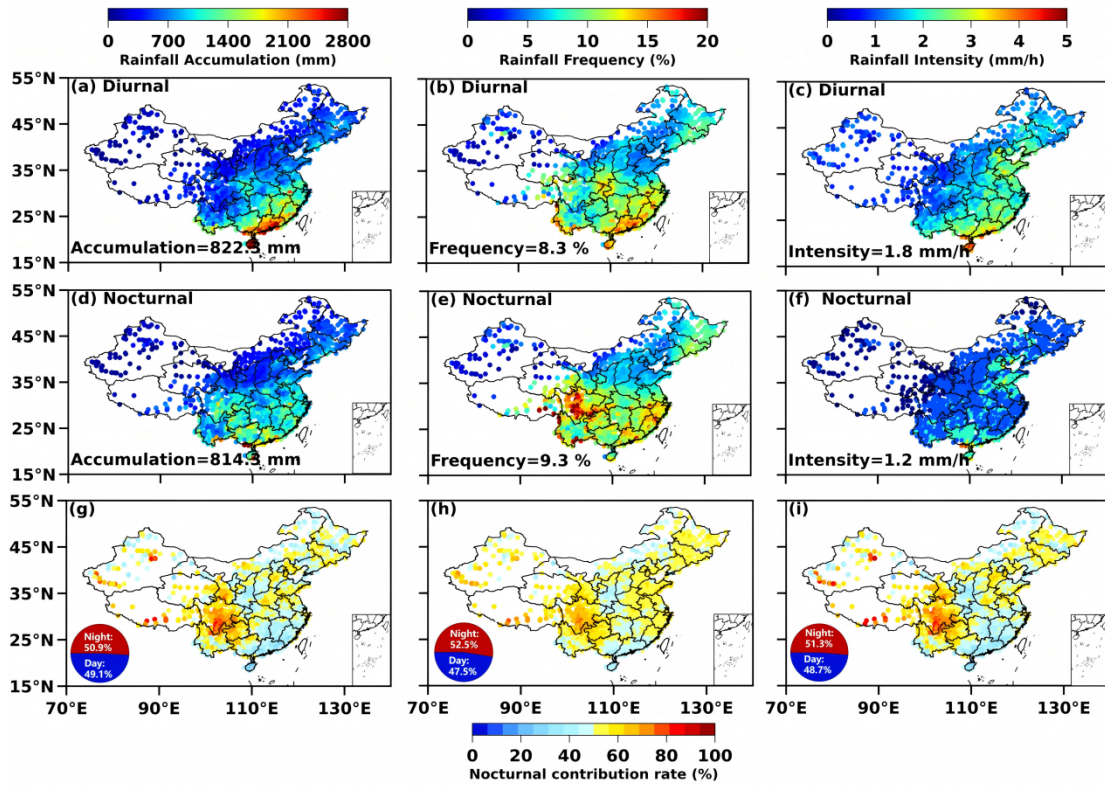
911

912

913

914

915

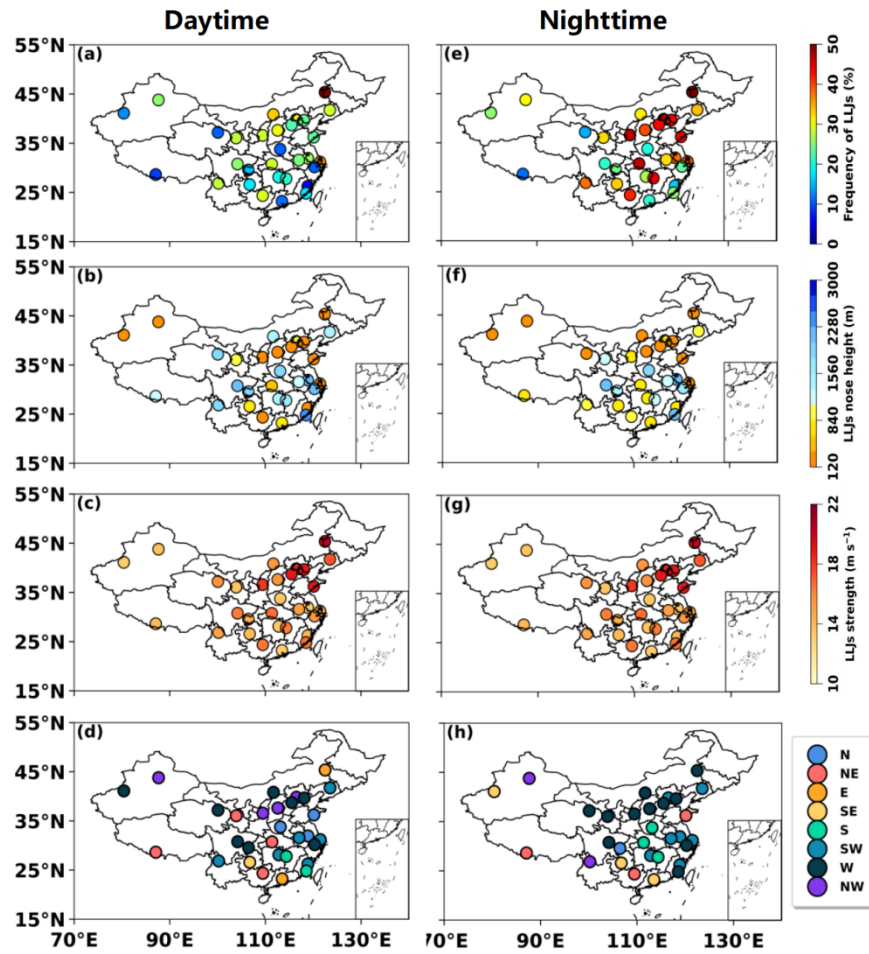


916

917 Figure 2. (a–c) Spatial distributions of accumulated rainfall (mm), rainfall frequency  
 918 (%) and rainfall intensity (mm/h) in the daytime from April to October in 2023–2024.  
 919 The numbers in the upper left corner represent the national average; (d–f) the same as  
 920 (a–c), but in the nighttime; (g–i) Nocturnal contribution ratios of accumulated rainfall,  
 921 frequency, and occurrence frequency of heavy rainfall (>75th percentile intensity). The  
 922 pie charts illustrate the relative contribution rates of daytime (blue) and nighttime (red)  
 923 at the national scale

924

925



926

927 Figure 3. (a–d) Spatial distribution of occurrence frequency, height, strength, and the  
 928 dominant wind direction of LLJs observed by 31 RWP stations during April–October  
 929 from 2023 to 2024 in the daytime. (e–h) Same as (a–d), but in the nighttime.

930

931

932

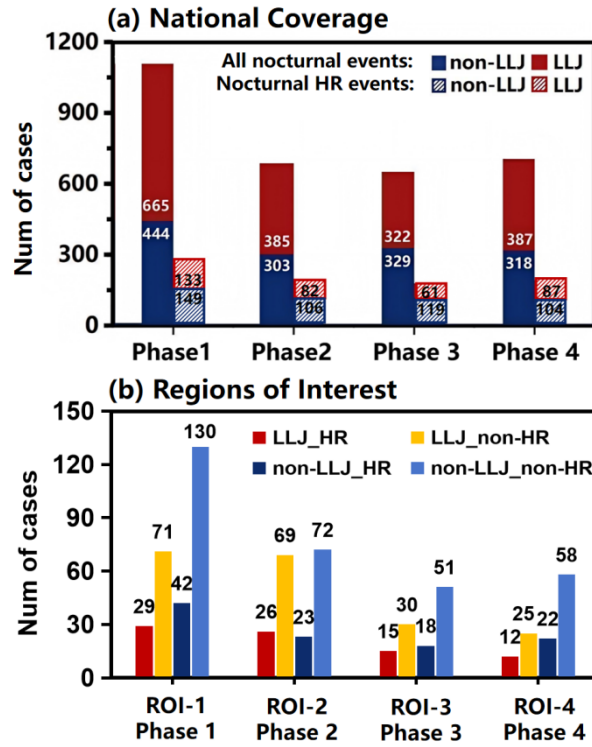
933

934

935

936

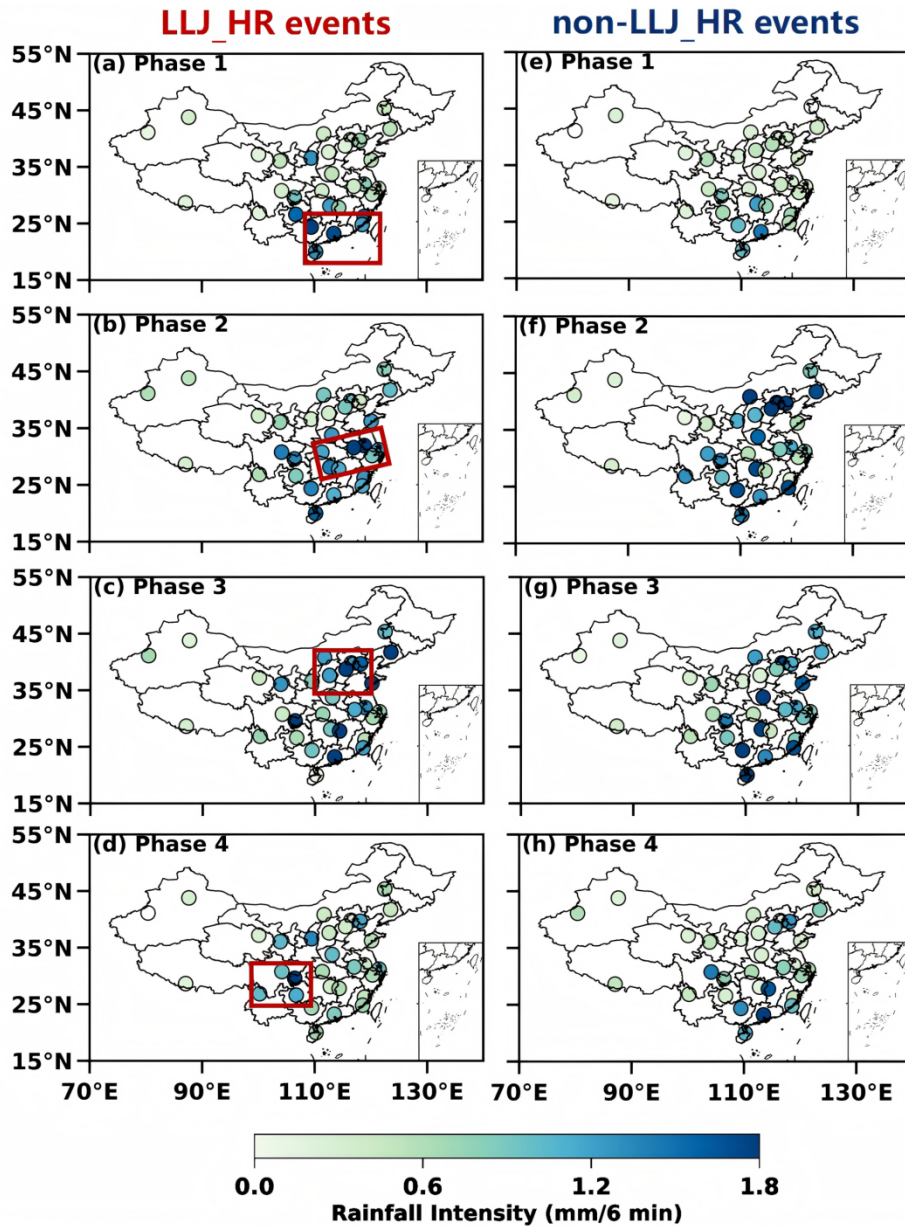
937



938

939 Figure 4. Statistics of all nocturnal rainfall events (solid-filled bars) and nocturnal heavy  
 940 rainfall (HR; diagonally striped bars) events across China during four phases,  
 941 categorized into LLJ events (red) and non-LLJ events (blue). (b) Statistics of nocturnal  
 942 rainfall events within the four ROIs (ROI-1 to ROI-4) during their corresponding  
 943 phases, categorized into four types: LLJ\_HR (red), LLJ\_non-HR (yellow), non-  
 944 LLJ\_HR (dark blue), and non-LLJ\_non-HR (light blue) events.

945

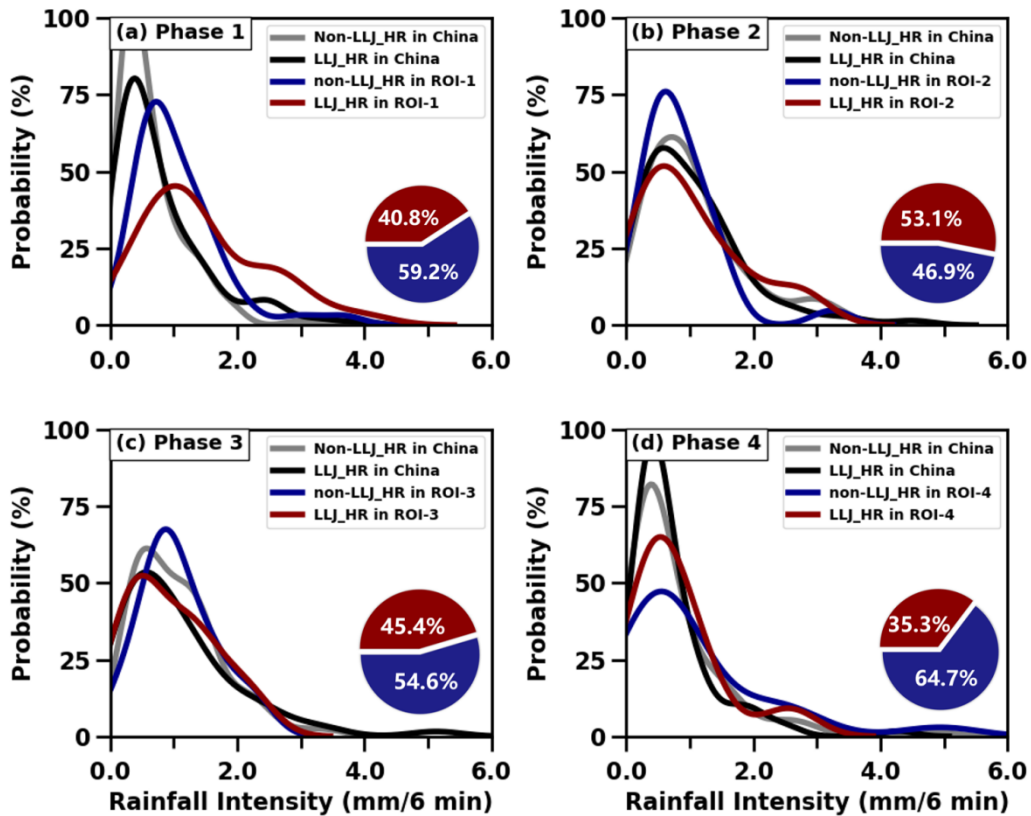


946

947 Figure 5. (a–d) Spatial distributions of site-averaged rain rate (mm/6 min) for nocturnal  
 948 LLJ\_HR events during the warm season from Phase 1 to Phase 4 across China; (e–h)  
 949 Same as (a–d), but for non-LLJ\_HR events. The red frame indicates four ROIs.

950

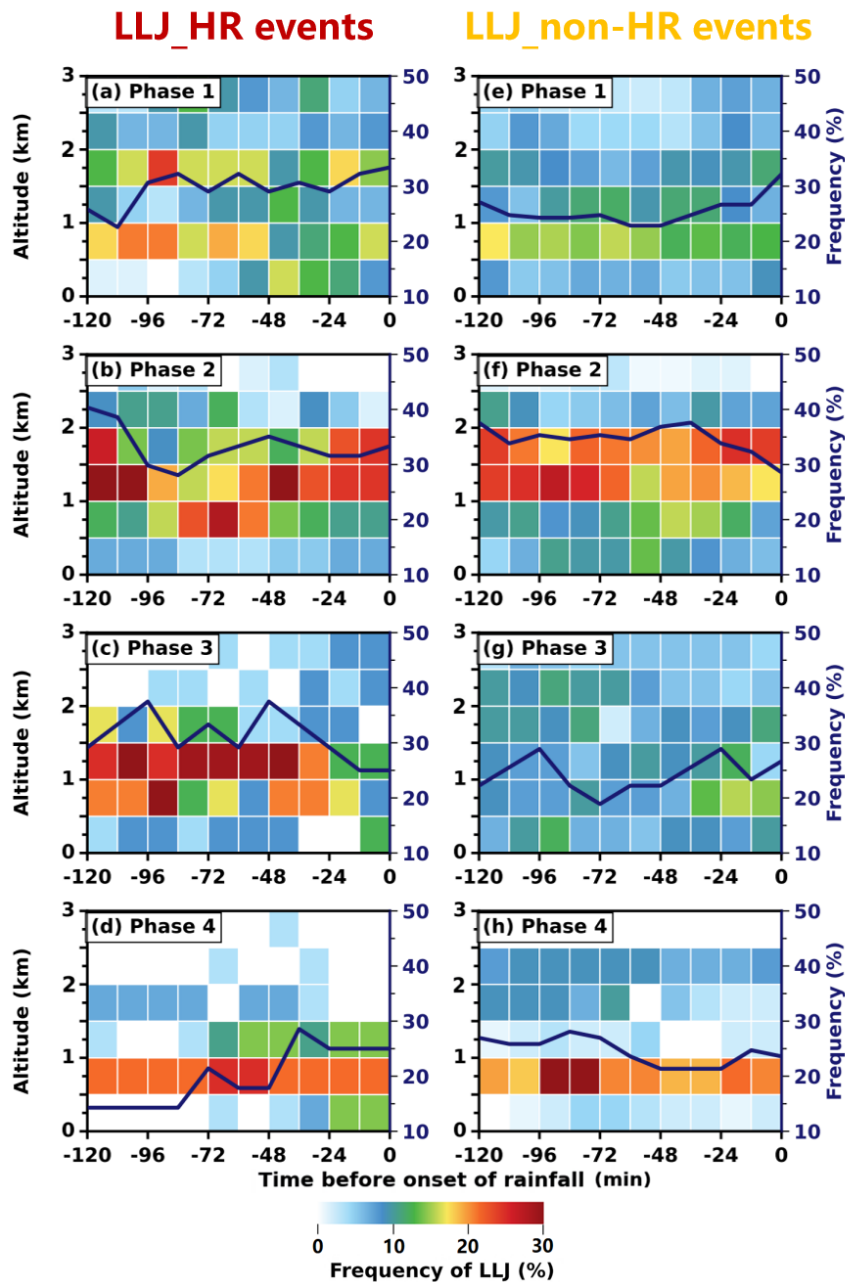
951



952

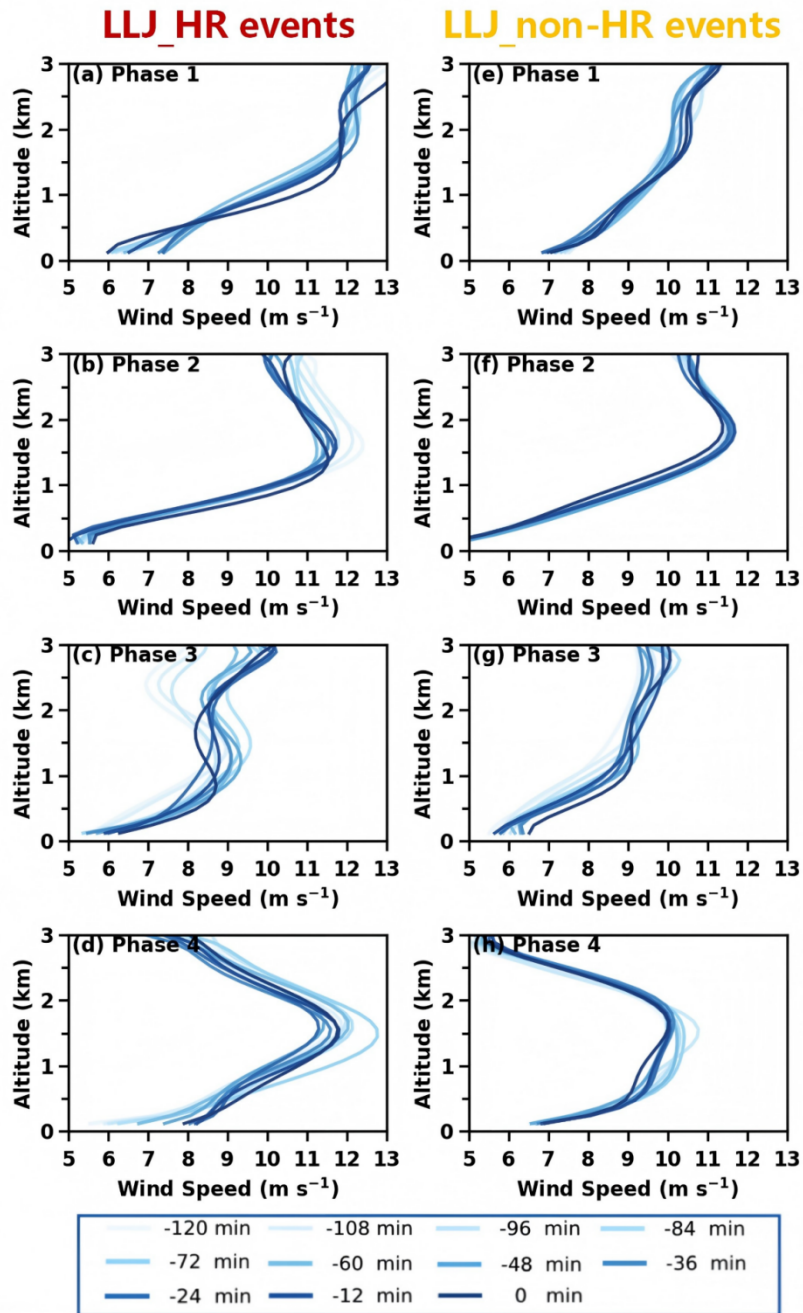
953 Figure 6. (a) Probability density distributions of average rain rate (mm/6 min) for  
 954 LLJ\_HR events (black solid lines) and non-LLJ\_HR events (gray solid lines) across  
 955 China during Phase 1, and specifically in ROI-1 for LLJ\_HR events (red solid lines)  
 956 and non-LLJ\_HR events (blue solid lines). (b-d) the same as panel (a), but for  
 957 comparisons between national-scale and other regional-scale events in ROI-2 during  
 958 Phase 2, ROI-3 during Phase 3, and ROI-4 during Phase 4. The pie chart at the lower  
 959 right shows the proportion distribution of LLJ\_HR (red) and non-LLJ\_HR (blue) events  
 960 in these key regions during each period

961



962

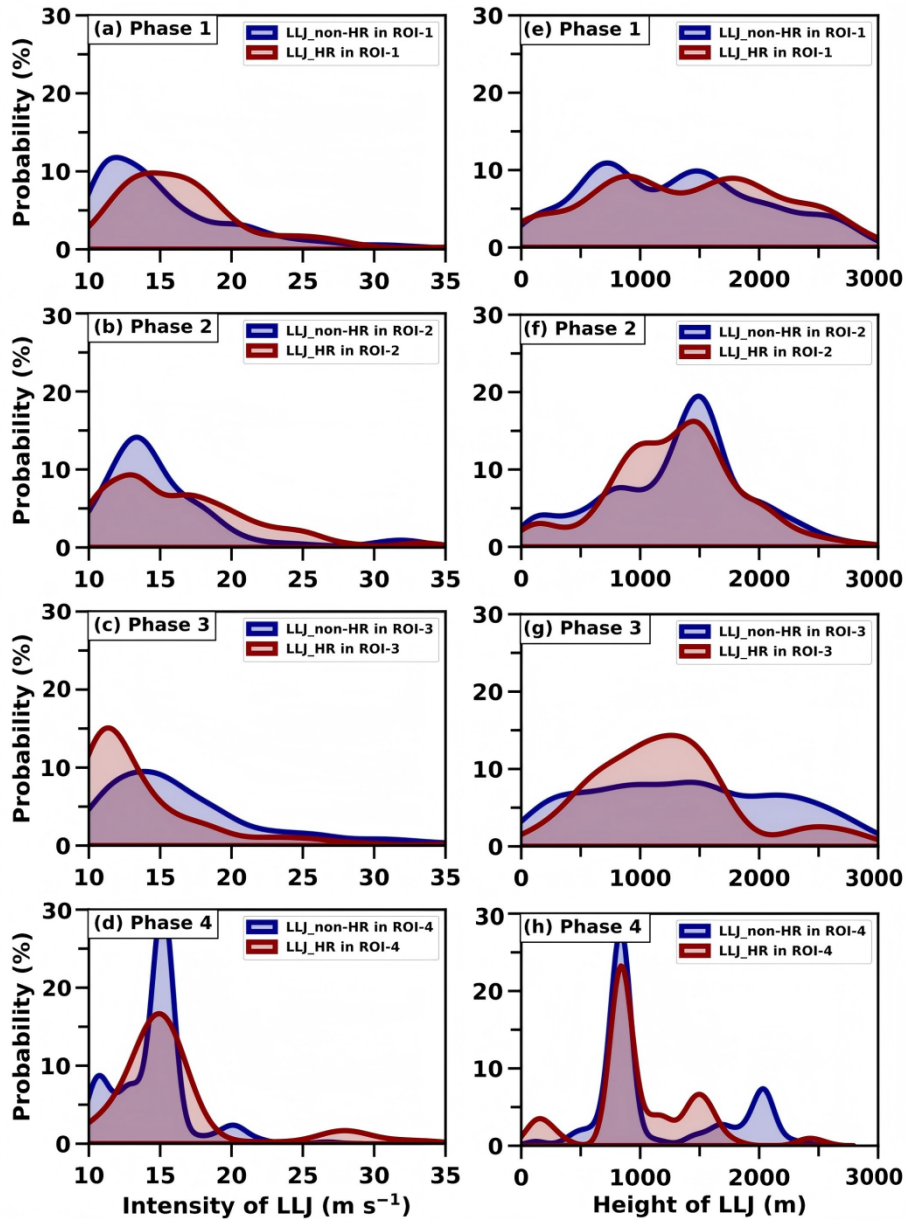
963 Figure 7. Time-height evolution of LLJ occurrence frequency (color shading, every 12  
 964 min, within 500 m vertical bins) detected by RWP with 2 hours preceding nocturnal  
 965 rainfall in LLJ\_HR events in (a) ROI-1 during Phase 1, (b) ROI-2 during Phase 2, (c)  
 966 ROI-3 during Phase 3, and (d) in ROI-4 during Phase 4. Dark blue solid lines denote  
 967 accumulated LLJ frequency over 0–3 km latitude. (e-h) Same as (a-d), but for LLJ\_non-  
 968 HR events



969

970 Figure 8. (a-d) Evolution of RWP-detected mean wind profiles of LLJs (blue solid lines,  
 971 every 12 min) within 2 hours preceding nocturnal rainfall in LLJ\_HR events in (a) ROI-  
 972 1 during Phase 1, (b) ROI-2 during Phase 2, (c) ROI-3 during Phase 3, and (d) in ROI-  
 973 4 during Phase 4. (e-h) Same as (a-d), but for LLJ\_non-HR events

974



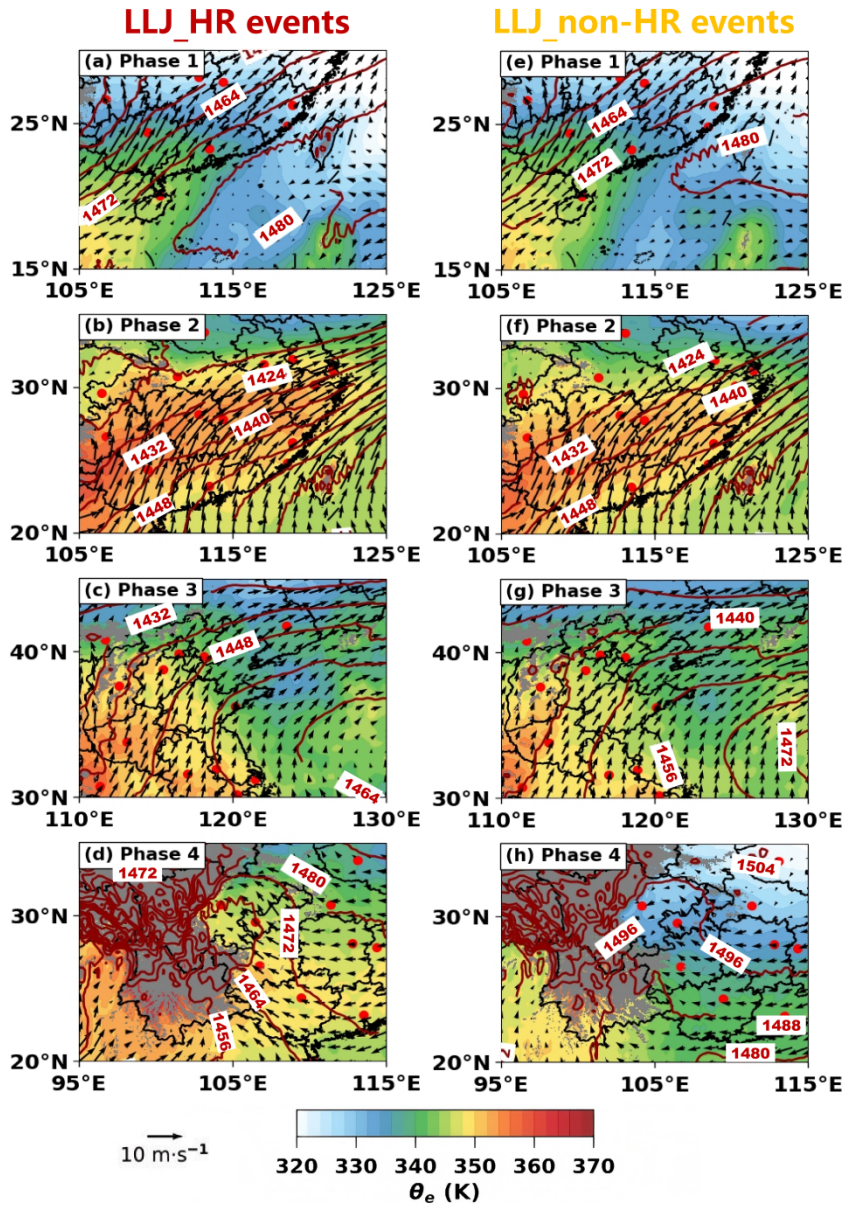
975

976 Figure 9. Probability density distributions of jet core intensity from RWP observations  
 977 within 2 hours preceding nocturnal rainfall in LLJ\_HR events in (a) ROI-1 during Phase  
 978 1, (b) ROI-2 during Phase 2, (c) ROI-3 during Phase 3, and (d) in ROI-4 during Phase  
 979 4. (e-h) Same as (a-d), but for the height of LLJs

980

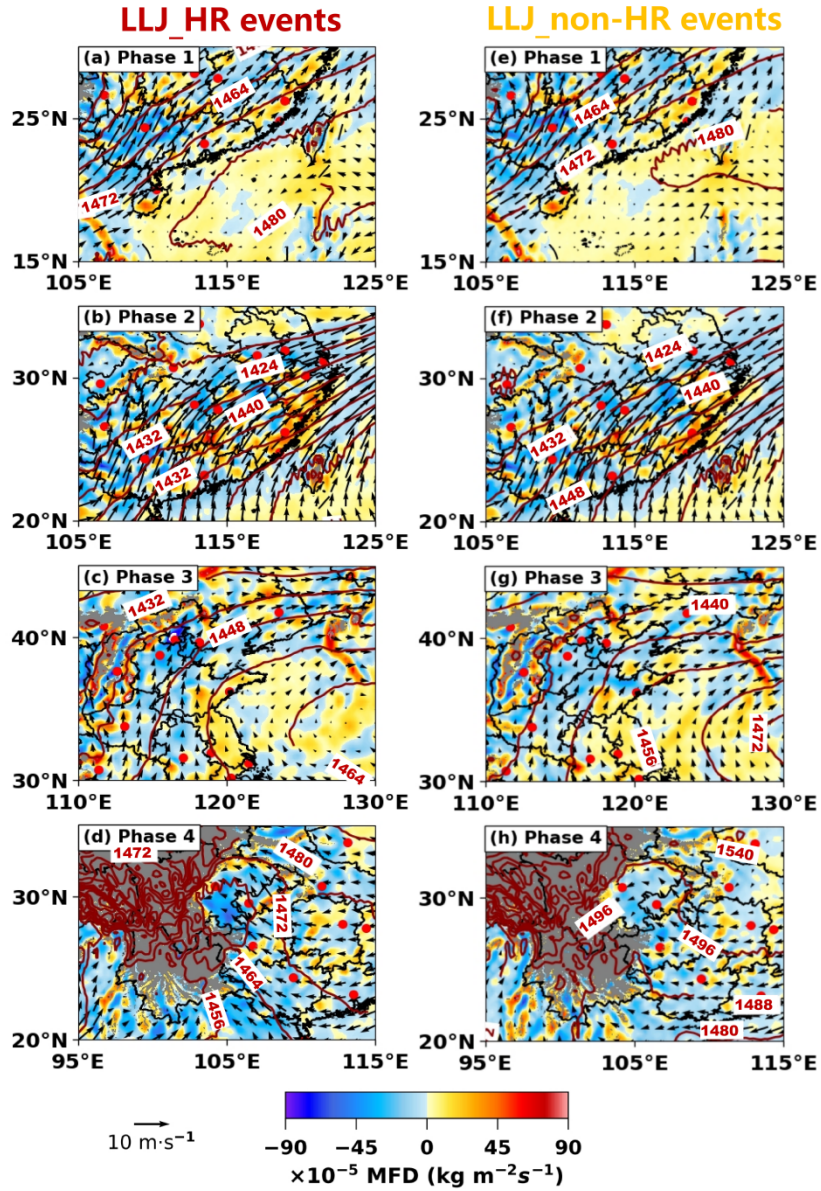
981

982



983

984 Figure 10. Distributions of equivalent potential temperature (shading, unit: K) at 850  
 985 hPa, superimposed with 850 hPa horizontal wind vectors (black arrows) and  
 986 geopotential height contours (red solid lines), for LLJ\_HR events within 1-hour time  
 987 window preceding nocturnal rainfall onset in (a) ROI-1 during Phase 1, (b) ROI-2  
 988 during Phase 2, (c) ROI-3 during Phase 3, and (d) in ROI-4 during Phase 4. Gray  
 989 shading denotes terrain elevation exceeding 850 hPa level. The reference vector (10  
 990 m s<sup>-1</sup>) is shown at the lower-left corner. (e-h) Same as (a-d), but for LLJ\_non-HR events



991

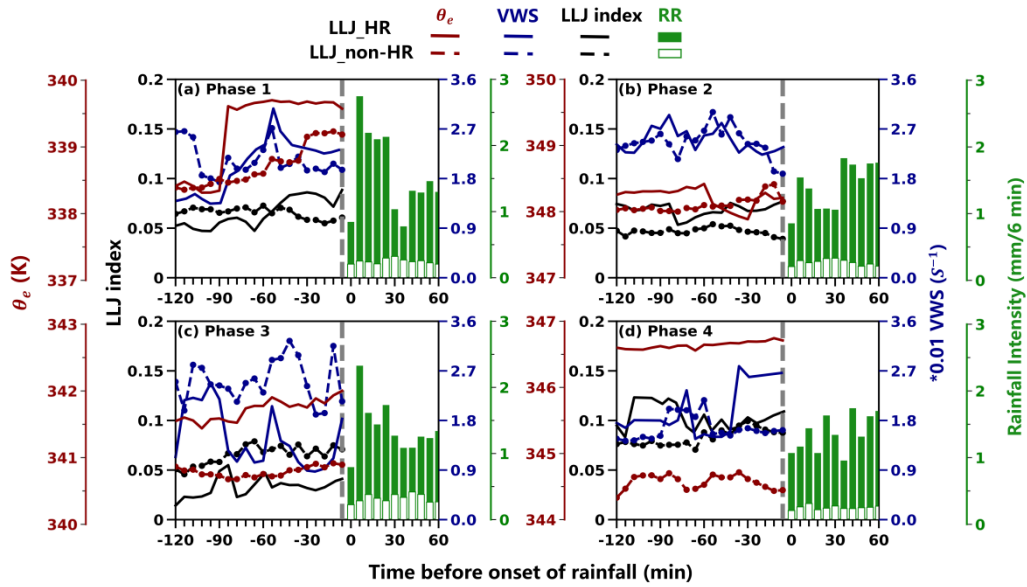
992 Figure 11. Same as Figure 10, but showing the integrated moisture flux divergence

993 (shading, unit:  $\text{kg m}^{-2} \text{ s}^{-1}$ ) between 1000–700 hPa at 1 hour prior to preceding

994 nocturnal rainfall onset

995

996



997

998 Figure 12. Temporal evolution of surface equivalent potential temperature ( $\theta_e$ , red  
 999 lines), vertical wind shear (VWS, blue lines), and LLJ index (black lines) averaged  
 1000 within 2 hours preceding nocturnal rainfall for LLJ\_HR events (solid lines) and  
 1001 LLJ\_non-HR events (dashed lines) in (a) ROI-1 during Phase 1, (b) ROI-2 during Phase  
 1002 2, (c) ROI-3 during Phase 3, and (d) in ROI-4 during Phase 4. Green bars denote 6-min  
 1003 averaged rain rate (mm/ 6 min) after LLJ\_HR (solid bars) and LLJ\_non-HR (open bars)  
 1004 events onset

1005

1006

1007

1008